NASA/TP—2000–210074

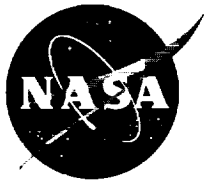

Effect of Crystal Orientation on Analysis of Single-Crystal, Nickel-Based Turbine Blade Superalloys

G.R. Swanson
Marshall Space Flight Center, Marshall Space Flight Center, Alabama

N.K. Arakere
University of Florida, Gainesville, Florida

February 2000

The NASA STI Program Office...in Profile

Since its founding, NASA has been dedicated to the advancement of aeronautics and space science. The NASA Scientific and Technical Information (STI) Program Office plays a key part in helping NASA maintain this important role.

The NASA STI Program Office is operated by Langley Research Center, the lead center for NASA's scientific and technical information. The NASA STI Program Office provides access to the NASA STI Database, the largest collection of aeronautical and space science STI in the world. The Program Office is also NASA's institutional mechanism for disseminating the results of its research and development activities. These results are published by NASA in the NASA STI Report Series, which includes the following report types:

- TECHNICAL PUBLICATION. Reports of completed research or a major significant phase of research that present the results of NASA programs and include extensive data or theoretical analysis. Includes compilations of significant scientific and technical data and information deemed to be of continuing reference value. NASA's counterpart of peer-reviewed formal professional papers but has less stringent limitations on manuscript length and extent of graphic presentations.

- TECHNICAL MEMORANDUM. Scientific and technical findings that are preliminary or of specialized interest, e.g., quick release reports, working papers, and bibliographies that contain minimal annotation. Does not contain extensive analysis.

- CONTRACTOR REPORT. Scientific and technical findings by NASA-sponsored contractors and grantees.

- CONFERENCE PUBLICATION. Collected papers from scientific and technical conferences, symposia, seminars, or other meetings sponsored or cosponsored by NASA.

- SPECIAL PUBLICATION. Scientific, technical, or historical information from NASA programs, projects, and mission, often concerned with subjects having substantial public interest.

- TECHNICAL TRANSLATION. English-language translations of foreign scientific and technical material pertinent to NASA's mission.

Specialized services that complement the STI Program Office's diverse offerings include creating custom thesauri, building customized databases, organizing and publishing research results...even providing videos.

For more information about the NASA STI Program Office, see the following:

- Access the NASA STI Program Home Page at ***http://www.sti.nasa.gov***

- E-mail your question via the Internet to help@sti.nasa.gov

- Fax your question to the NASA Access Help Desk at (301) 621–0134

- Telephone the NASA Access Help Desk at (301) 621–0390

- Write to:
  NASA Access Help Desk
  NASA Center for AeroSpace Information
  7121 Standard Drive
  Hanover, MD 21076–1320

NASA/TP—2000–210074

Effect of Crystal Orientation on Analysis of Single-Crystal, Nickel-Based Turbine Blade Superalloys

G.R. Swanson
Marshall Space Flight Center, Marshall Space Flight Center, Alabama

N.K. Arakere
University of Florida, Gainesville, Florida

National Aeronautics and
Space Administration

Marshall Space Flight Center

February 2000

Available from:

NASA Center for AeroSpace Information
7121 Standard Drive
Hanover, MD 21076–1320
(301) 621–0390

National Technical Information Service
5285 Port Royal Road
Springfield, VA 22161
(703) 487–4650

TABLE OF CONTENTS

LIST OF FIGURES

LIST OF FIGURES (Continued)

LIST OF FIGURES (Continued)

LIST OF TABLES

LIST OF ACRONYMS AND SYMBOLS

Al	aluminum
AT	alternate turbopump
C	carbon
Cr	chromium
CDR	critical design review
DOF	degreee of freedom
FCC	face centered cubic
FCG	fatigue crack growth
FE	finite element
FEM	finite element model
HCF	high-cycle fatigue
HIP	hot isostatic pressing
HPFTP	high-pressure fuel turbopump
LCF	low-cycle fatigue
Ni	nickel
PWA	Pratt and Whitney Aircraft
RPL SL	rated power level service life
SSME	Space Shuttle Main Engine
Ta	Tantalum

TECHNICAL PUBLICATION

EFFECT OF CRYSTAL ORIENTATION ON ANALYSIS OF SINGLE-CRYSTAL NICKEL-BASED TURBINE BLADE SUPERALLOYS

1. FATIGUE FAILURE OF SINGLE-CRYSTAL NICKEL SUPERALLOYS

1.1 Introduction

High-cycle fatigue (HCF)-induced failures in aircraft gas-turbine engines is a pervasive problem affecting a wide range of components and materials. HCF is currently the primary cause of component failures in gas turbine aircraft engines,[1] as shown in figure 1. Furthermore, blades are the components most likely to fail by HCF, as shown in figure 2. Turbine blades in high-performance aircraft and rocket engines are increasingly being made of single-crystal nickel (Ni) superalloys. Single-crystal Ni-based superalloys were developed to provide superior creep, stress rupture, melt resistance, and thermomechanical fatigue capabilities over polycrystalline alloys previously used in the production of turbine blades and vanes. Currently, the most widely used single-crystal turbine blade superalloys are Pratt and Whitney Aircraft (PWA) 1480 and PWA 1484.[2] These alloys play an important role in commercial, military, and space propulsion systems. PWA 1493, identical to PWA 1480 but with tighter chemical constituent control, is used in the NASA Space Shuttle Main Engine (SSME) alternate turbopump (AT), a liquid hydrogen-fueled rocket engine.

Single-crystal materials differ significantly from polycrystalline alloys in that they have highly orthotropic properties, making the position of the crystal lattice relative to the part geometry a significant factor in the overall analysis.[3] Currently, no analytical codes exist that can accurately predict crack growth for materials with orthotropic properties. Current computer codes generate stress intensity factor predictions for a given stress field based on isotropic assumptions. Material testing data must then be tailored to this condition to determine a reasonable assessment of fatigue capability. The modified Goodman approach currently used for component design does not address important factors that affect HCF such as fretting and/or galling surface damage, and interaction with low-cycle fatigue (LCF).[1] Blade-disk attachment areas are particularly prone to fretting/galling fatigue damage.[2] Rocket engine service presents another set of requirements that shifts emphasis to low-temperature fatigue and fracture capability with particular attention given to thermal, cryogenic, and high-pressure hydrogen gas exposure.[2] To address HCF-induced component failures, the gas turbine industry, NASA, the U.S. Air Force, and U.S. Navy have made significant efforts in understanding fatigue in single-crystal turbine blade superalloys. Understanding fatigue initiation, threshold, and region II fatigue crack growth are of primary importance, and there is great need for improvements in fracture mechanics properties of turbine blade alloys. The need to apply damage-tolerant concepts to single-crystal Ni superalloy components is imminent.[2] While a large amount of data have been collected, there currently is no simple method for applying this knowledge toward the design of more robust gas turbine engine components. It is therefore essential to develop failure criteria for single crystals, based on available fatigue and fracture test data, that will permit a designer to utilize the lessons learned.

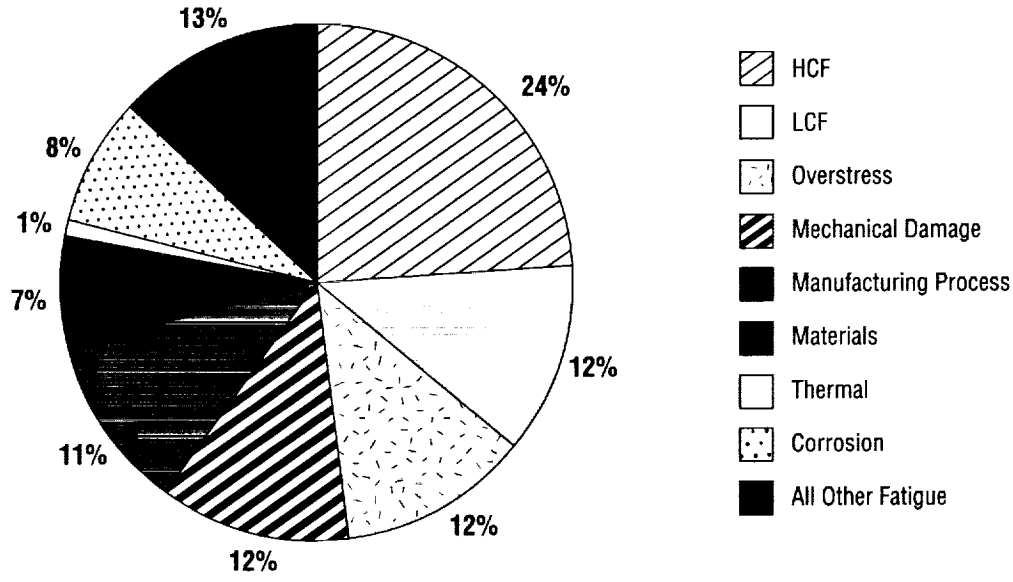

Figure 1. Representative jet engine component distress mode statistics.[1]

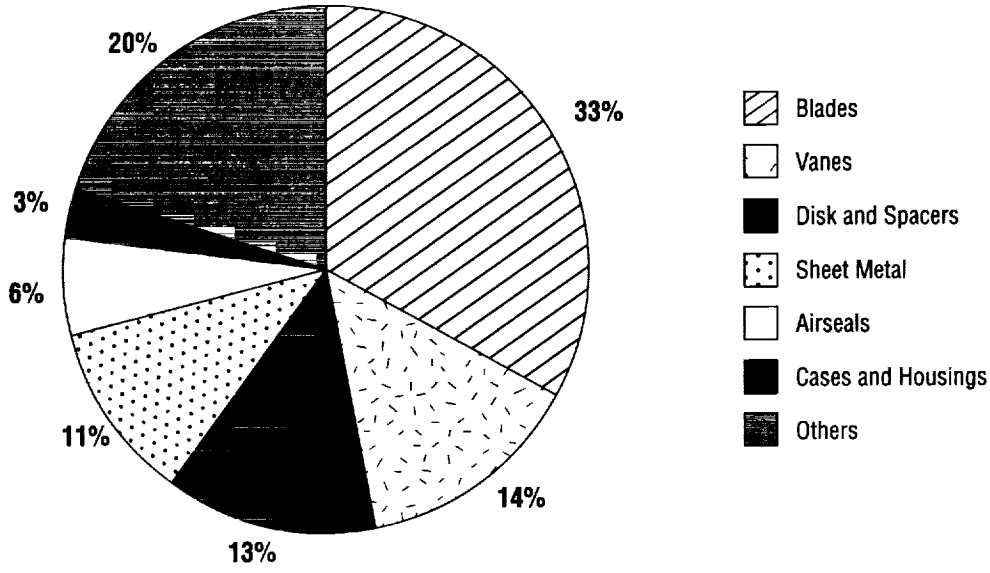

Figure 2. Representative distribution of HCF problems by component.[1]

1.2 Research Objectives

Objectives for this study, enumerated below, are motivated by the need for developing failure criteria and fatigue life evaluation procedures for high-temperature, single-crystal components using available fatigue data and finite element modeling of turbine blades:

1. Provide a brief overview of the macrostructure, microstructure, and manufacture of single-crystal castings.

2. Give a brief description of fatigue crack initiation and crack growth mechanisms, based on available test data.

3. Develop fatigue failure criteria for single-crystal material by suitably modifying failure criteria for polycrystalline material. Apply the proposed criteria for uniaxial LCF test data to determine the most effective failure parameter. Determine a lifing equation based on the curve fit of the failure parameter with LCF test data.

4. Describe finite element modeling of single-crystal SSME turbine blades, including the effects of variation of primary and secondary crystal orientations.

5. Using the finite element (FE) stress analysis results and the fatigue life relations developed, determine the effect of variation of primary and secondary crystal orientations on life at critical blade locations.

6. Determine the most advantageous secondary crystal orientation for a given blade design.

2. SINGLE-CRYSTAL NICKEL SUPERALLOYS

2.1 Introduction

Turbine operating temperatures have steadily climbed from ≈1,600 °F in the 1960's to the present day 3,000 °F to meet demands for higher engine efficiencies. Single-crystal Ni-based superalloys were developed to provide superior creep, stress rupture, melt resistance, and thermomechanical fatigue capabilities over polycrystalline alloys previously used in the production of turbine blades and vanes.

Grain boundaries are typically the weak link in high-temperature materials, providing passages for diffusion and oxidation, with failures generally originating at these locations. Grain boundary strengtheners are added to the alloy chemistry in an effort to increase capability. The strengtheners have the adverse effect of lowering the melting point of the alloy. The intent in the manufacture of single-crystal components is to produce a part from one large grain. Elimination of grain boundaries and grain boundary-strengthening elements results in improved high-temperature fatigue and creep capabilities.[4]

2.2 Microstructural Properties

Ni-based single-crystal superalloys are precipitation-strengthened cast monograin superalloys based on the Ni-Cr-Al system. The macrostructure of this material is characterized by parallel, continuous primary dendrites spanning the casting, without interruption, in the direction of solidification. Secondary dendrite arms (perpendicular to solidification) define the interdendritic spacing. Solidification for both primary and secondary dendrite arms proceeds in the <001> family of directions. Carbides, undissolved eutectic pools, and associated microporosity are concentrated in the interdendritic regions. These features represent microstructural discontinuities, and often exert a controlling influence on the fatigue crack initiation behavior of the alloy.[2] The microstructure consists of ≈60 percent by volume of γ' precipitates in a γ matrix. The γ' precipitate, based on the intermetallic compound Ni_3Al, is the strengthening phase in Ni-based superalloys. These alloys obtain their high-temperature strength from the presence of the γ' precipitate phase within the primary γ matrix. The γ' precipitate is a face centered cubic (FCC) structure and composed of the intermetallic compound Ni_3Al. The γ' precipitate is suspended within the γ matrix, which is also of FCC structure and comprised of Ni with cobalt, chromium, tungsten, and tantalum in solution. Figure 3 shows a schematic diagram of the γ' phase within the γ matrix.[3] The cuboidal γ' precipitate ranges in size from 0.35 to 0.6 μm as shown in figure 4.[2] At low to intermediate temperatures the γ' precipitate does not allow dislocation bypass and hence forces the shearing of the precipitate in order for a dislocation to move through the γ matrix.[2] Shearing of the γ' precipitate relative to the γ matrix requires significantly higher energy, resulting in a stronger material.

Material properties of the single-crystal alloy is controlled by the dispersion of the γ' precipitate in the γ matrix. Cooling rate is controlled to be very low during the single-crystal casting process. This gives the γ' time to precipitate out and grow. The net result is a γ matrix containing very coarse γ'. Significant gaps exist within the γ matrix precipitate leaving avenues for dislocations to propagate, resulting in a degradation of overall material properties. To eliminate these avenues and provide a more uniform

distribution of γ' precipitates, a solution heat treat is performed. After casting, the parts are brought up to a temperature where the γ' goes back into a solution. The parts are then cooled very rapidly, permitting the γ' to precipitate out but not allowing it to grow, resulting in a microstructure with a fine dispersion of fine cuboidal γ' precipitate. Since grain boundary strengtheners are not added to single-crystal alloys, the solution heat treat process can be conducted at 150 °F higher than that attainable with polycrystalline materials. This increased temperature capability permits complete solutioning of the coarse γ' that is not possible with the other materials. The complete solutioning and fine dispersion of γ' in the γ matrix gives single-crystal alloys their improved high-temperature material capabilities.[3]

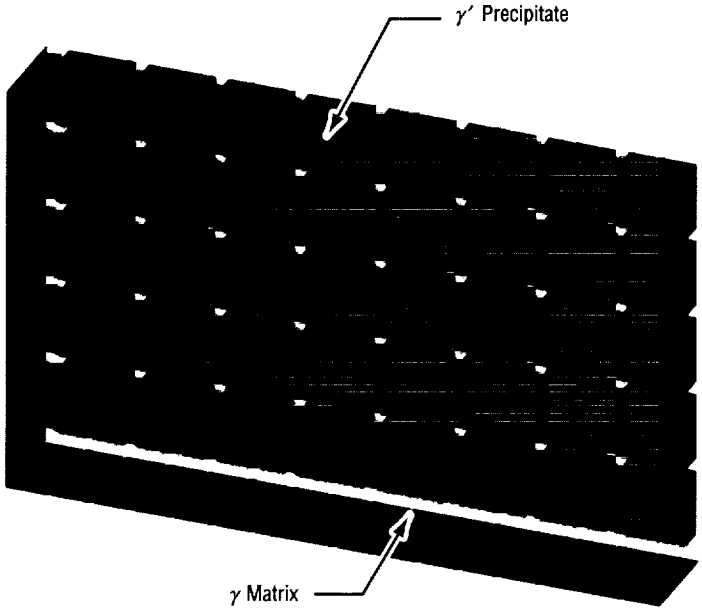

Figure 3. Schematic of the γ' precipitate in a γ matrix.[3]

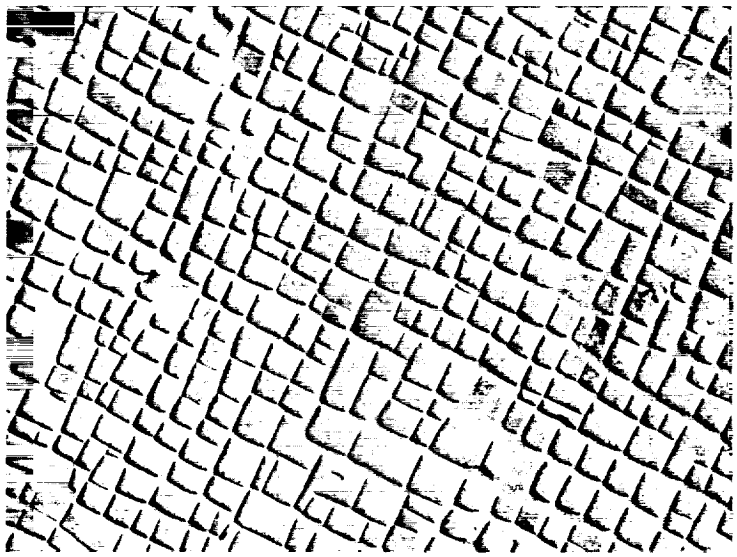

Figure 4. Cuboidal γ' precipitates (0.35–0.6 μm) in PWA 1480.[2]

2.3 Crystallographic Orientation

Single-crystal superalloys have highly orthotropic material properties that vary significantly with direction relative to the crystal lattice. Material testing is typically performed for loading applied along a number of different crystallographic orientations to ascertain minimum and maximum properties for the alloy. Display of experimental data is done by defining the crystallographic plane normal to direction of applied load during testing.

The majority of material testing focuses on two key crystallographic orientations, <001> and <111>, which have the largest variation in capabilities relative to each other. Elastic modulus in the <001> direction is at a minimum for the alloy. Planes normal to each other such as <001>, <100>, and <010> possess identical material properties (fig. 5). There is not a significant amount of data available for other crystallographic orientations. Material testing data indicate that maximum creep capability is attained for loading in the <001> direction. Orientation of the crystal lattice relative to the turbine blade geometry is driven by these data. Primary crystallographic orientation of a turbine blade, commonly referred to as α, is defined as the relative angle between the airfoil stacking line and the <001> direction. Current manufacturing capability permits control of α to within 5° of the stacking line. The SSME AT blades are allowed to have a maximum α variation of 15°.

Secondary orientation, commonly referred to as β, defines the angle of the <100> orientation relative to the blade geometry. Typically, the reference location on the blade geometry for establishing 0° β is a line parallel to the blade attachment, as shown in figure 6. Establishment of a preferred β for a blade design is not governed by the strict rules that determine the required α. In most turbine blade castings, the secondary orientation β is neither specified nor controlled during the manufacturing process. The β orientation for a given blade casting, therefore, becomes a random variable. However, the β orientation for each blade usually is recorded after the casting process is complete. Because each blade can have a different secondary orientation, finite element stress analysis of the blades has to account for a range of β orientations between 0° and 90°. Control of secondary orientation has the potential to add structural margin to a design without an increase in part cost or weight.[3]

2.4 Manufacturing of Single-Crystal Turbine Blades

Single-crystal Ni superalloy turbine components are produced using a high-gradient investment casting process. Two key areas where the manufacturing process for single-crystal castings differ from polycrystalline castings are the construction of the ceramic mold and the solidification of the alloy during the actual casting operation.

Fabrication of a wax injection die is the first step in the overall process. Once the die is complete, wax or plastic is injected to produce a pattern reflecting the desired geometry. Turbine blades produced for use in high-pressure turbines typically require hollow cavities for supplying coolant air. To create these cavities, a ceramic core is introduced during the injection process. The wax is injected around the core, producing a cavity when it is removed, following solidification of the alloy. Once the patterns have been injected, they are assembled into a mold. At this point, the processing for single-crystal parts diverges from that of polycrystalline parts. A grain selector feature is added to each pattern prior to assembly into the mold. This selector feature establishes the primary and secondary crystallographic orientations of the finished part.

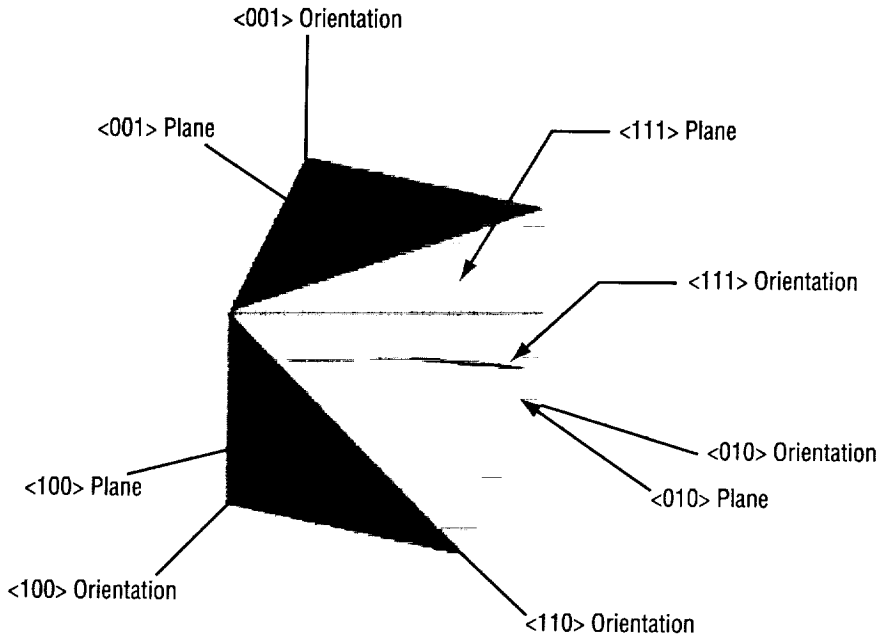

Figure 5. FCC crystallographic orientation.[3]

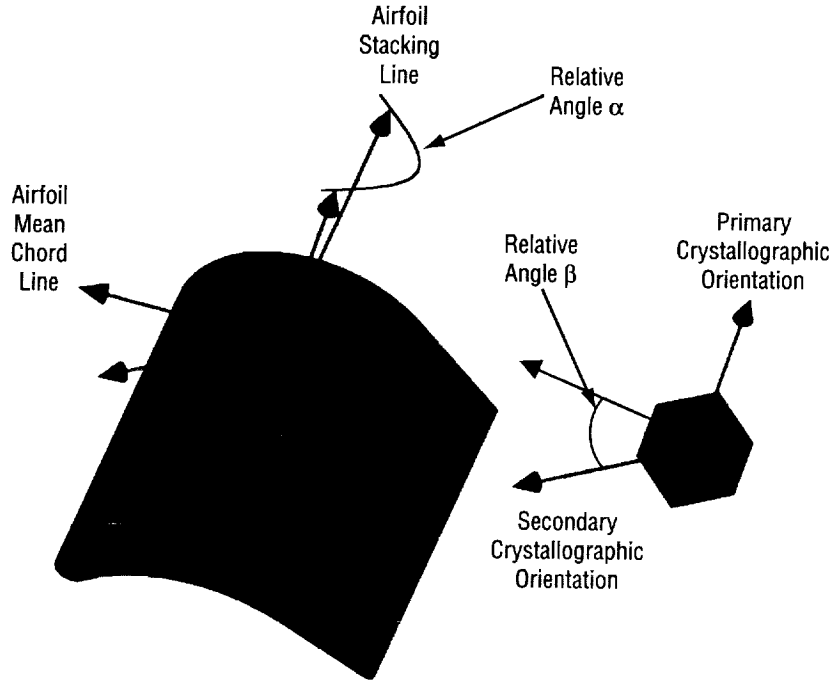

Figure 6. Convention for defining crystal orientation in turbine blades.[3]

Two methods for grain selection are currently utilized throughout the casting industry. One is through the use of a gate or blocker selector. Typically this is a helix or an elbow, as shown in figure 7, and operates on the principal of culling the forest of grains until only one is capable of continuing past the bottleneck. Blocker selectors are only capable of controlling the primary orientation. Use of crystal seeds is the other method utilized and has the ability to control both primary and secondary orientations. These seeds are actual pieces of the crystal cut from bars with known grain orientations. When the molten alloy contacts the seed and begins solidification, it assumes the seed lattice structure and continues to grow along the same orientation.

Upon completion of assembly, a ceramic shell is constructed around the wax patterns. This shell is fabricated by dipping the pattern into liquid slurry and then dusting it with a silica particulate. Several layers of dip coats and particulate are applied to give the mold strength. For polycrystalline parts, the shell completely encapsulates the pattern. Holes for the introduction of alloy into the mold and vents to permit entrapped air to escape are the only openings present in the shell structure. In addition to these standard openings, the entire bottom of the single-crystal pattern remains uncoated with the ceramic shell. After drying for several days, the molds are placed in an autoclave which utilizes temperature and steam to melt and remove the wax. Removal of the wax creates a hollow cavity that creates the desired part geometry when filled with alloy. Investment casting is commonly referred to as the lost wax casting process. Ceramic cores introduced at the time of pattern injection are not affected by the dewax operation and remain in the mold to create the required hollow cavities in the finished part.

Molds enter the foundry following dewax for the actual casting operation. At this point the processing of single and polycrystalline methods significantly differ. Polycrystalline molds are heated to near the melt temperature of the alloy while the alloy itself is brought to a temperature $\approx$20 °F above its melting point. The alloy is introduced into the mold under vacuum and the mold is quickly removed from the furnace. Solidification of the alloy initiates at all surfaces of the mold and rapid cooling is induced to minimize grain growth. A fine grain structure is the primary goal in polycrystalline alloys due to the superior fatigue capability over a coarse grain size. Processing operations for molds producing single-crystal hardware follow a different methodology, as shown in figure 8.

Molds are placed in the casting furnace at room temperature with the open bottom end setting on a copper plate. Water is circulated through the plate as the mold is heated past the incipient melt temperature of the alloy. Once at temperature, the alloy is added to the mold under vacuum. Solidification occurs instantly when the molten metal contacts the chill plate. For seeded parts, the chill plate prevents the seed from melting as the mold is heated; solidification initiates when the molten alloy contacts the cold seed.

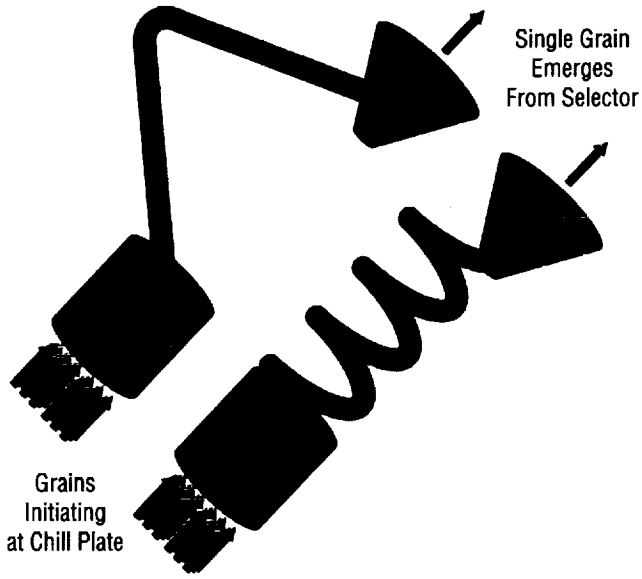

Figure 7. Typical blocker style crystal selectors.[3]

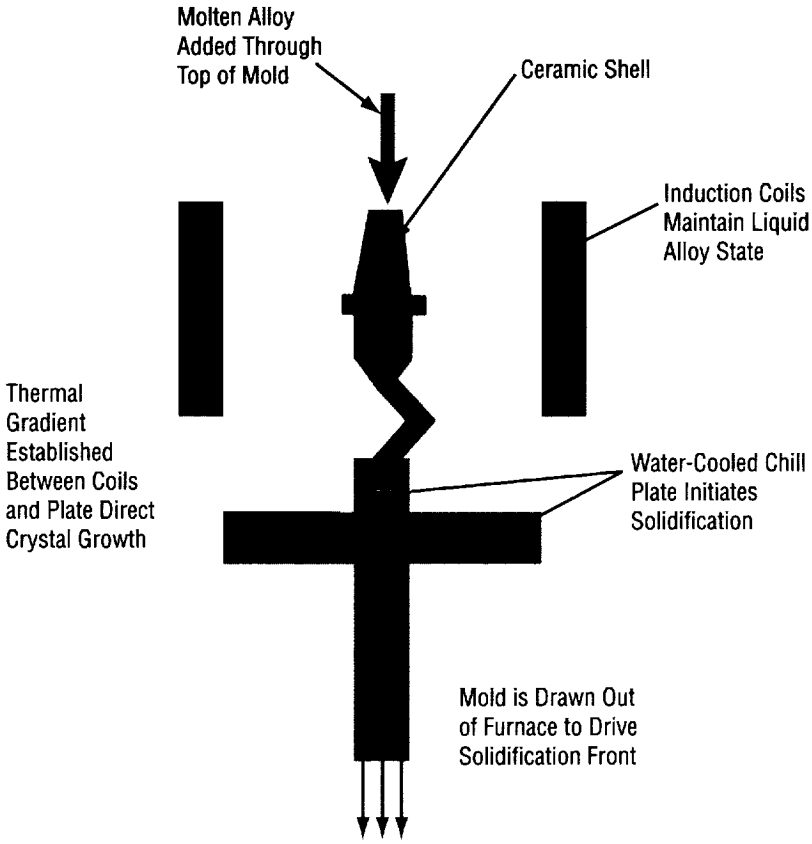

Figure 8. High-gradient single-crystal casting process.[3]

Heat is continually applied to the mold using an induction coil to maintain the mold temperature above the alloy incipient melt temperature. Grain growth occurs in the direction of the temperature gradient established between the chill plate and the induction coil. Initial solidification occurs at the chill plate interface only with the remainder of the mold maintained above the alloy melt temp. On nonseeded parts, these crystals initially have random orientations. Crystals with <001> orientations in the direction of the thermal gradient grow faster, overtaking those of other orientations to the grain selector. Seeded parts start out with the desired orientation transferred from the seed. Solidification of the complete mold is accomplished by slowly withdrawing the mold from the induction heat source, allowing the mold to cool from the chill plate up. The thermal gradient is maintained to encourage crystal growth in the correct orientation and prevent nucleation of grains elsewhere in the mold. This process is commonly designated a high-gradient process in reference to the large thermal gradient utilized to drive crystal growth. At the completion of the drawdown cycle, solidification of the mold is complete and it is removed from the furnace.

Subsequent operations involve removal of the ceramic shell from the parts and extraction of any cores used to produce internal cavities. Core removal is accomplished through use of a caustic solution that breaks down the binder holding the silica particulate together. Once the binder has been removed, the cores turn to very fine silica dust which is easily removed. Parts are subjected to a solution heat treatment to create the required γ' fine microstructure. Final finishing and inspections are completed prior to shipment.

3. FATIGUE FAILURE CRITERIA FOR SINGLE-CRYSTAL NICKEL SUPERALLOYS

3.1 Introduction

The fatigue failure modes in single-crystal Ni superalloys are dependent upon the prevalent active slip systems and dislocation mechanisms, which in turn depend on the microstructure, temperature, and environmental conditions. A very brief overview of deformation mechanisms, crack initiation, and crack propagation modes in FCC single crystals is described first. Adaptation of some fatigue failure theories used for polycrystalline materials to FCC single-crystal material is described next.

3.2 Deformation Mechanisms

Deformation mechanisms in single crystals are primarily dependent on microstructure, orientation, temperature, and crystal structure. Crystalline metals deform primarily due to the propagation of dislocations through the crystal lattice, when the temperature is less than about half the absolute melting point of the material. Deformation by dislocation climb, a diffusion-controlled process, becomes more important at higher temperatures.[4] Twinning is generally less important since resulting strains are very small compared to slip or climb. Slip in metal crystals often occurs on planes of high atomic density in closely packed directions because these planes generally correspond to the lowest possible energy for slip. The four octahedral planes corresponding to the high-density planes in the FCC crystal are shown in figure 9. Each octahedral plane has six slip directions associated with it. Three of these are termed easy slip or primary slip directions and the other three are secondary slip directions. Thus, there are 12 primary and 12 secondary slip directions associated with the four octahedral planes.[4] In addition, there are six possible slip directions in the three cube planes, as shown in figure 10. At low to intermediate temperatures, slip is likely to occur on the four close-packed octahedral planes in one of the 12 primary directions. At high temperatures, slip has been observed in nonclose-pack directions on the octahedral and cube planes, in an FCC crystal. Table 1 shows the 30 possible slip systems in an FCC crystal.[4]

Deformation mechanisms operative in PWA 1480 are divided into three temperature regions.[5] In the low-temperature regime (26 to 427 °C (79 to 800 °F)) the principal deformation mechanism is by (111)/<110> slip, and hence fractures produced at these temperatures exhibit (111) facets. Above 427 °C (800 °F), thermally activated cube cross slip is observed which is manifested by an increasing yield strength up to 871 °C (1,600 °F) and a proportionate increase in (111) dislocations that have cross slipped to (001) planes. Thus, Ni-based FCC single-crystal superalloys slip primarily on the octahedral and cube planes in specific slip directions. Elastic response of FCC crystals is obtained by expressing Hooke's law for materials with cubic symmetry and is explained in section 4. To model the global inelastic strain, slip on the individual slip planes has to be summed. The constitutive model for the inelastic strain response is then constructed from a relationship between the stress and slip on the slip planes.[4]

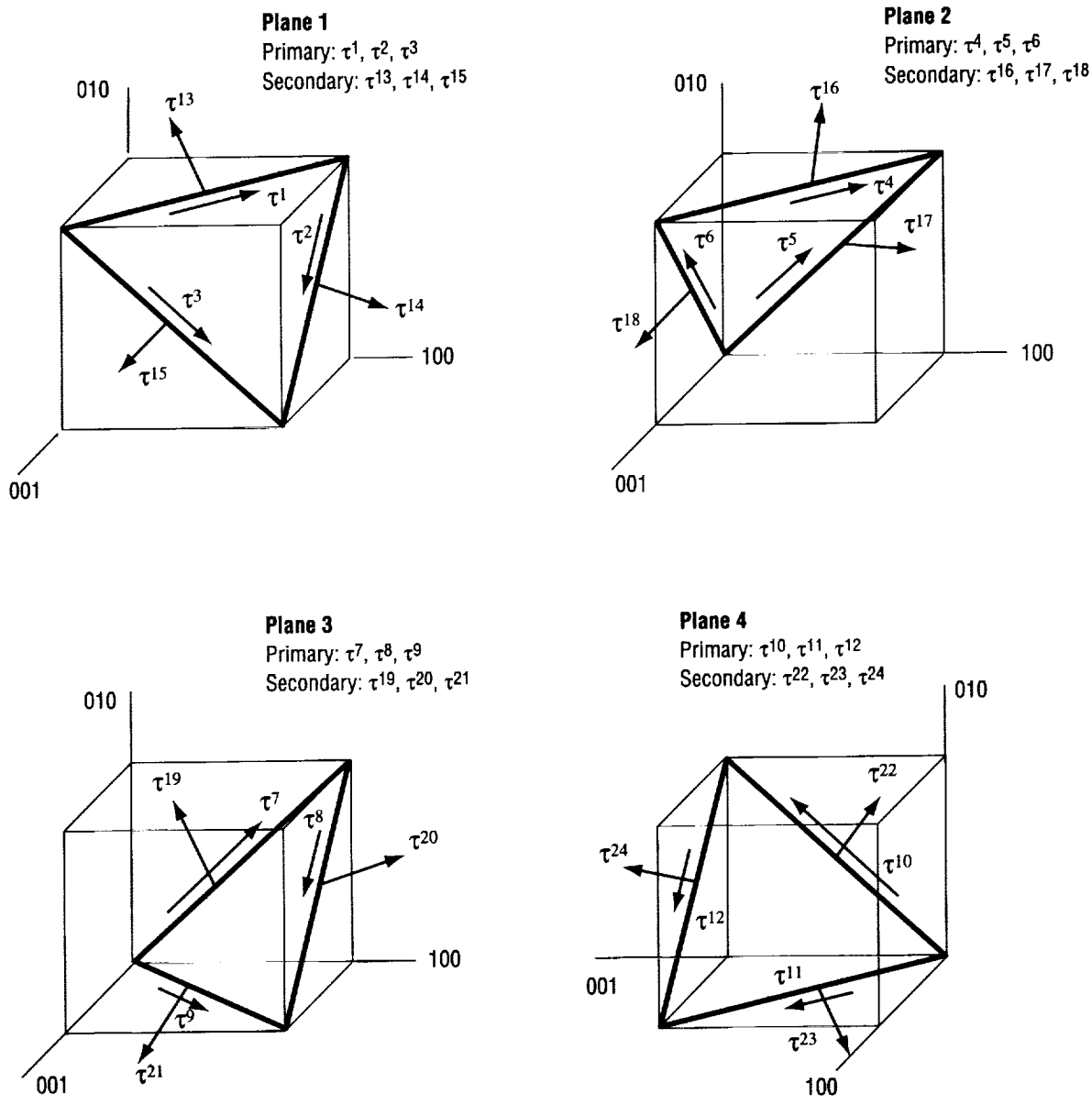

Figure 9. Primary (close-pack) and secondary (nonclose-pack) slip directions on the octahedral planes for an FCC crystal.[4]

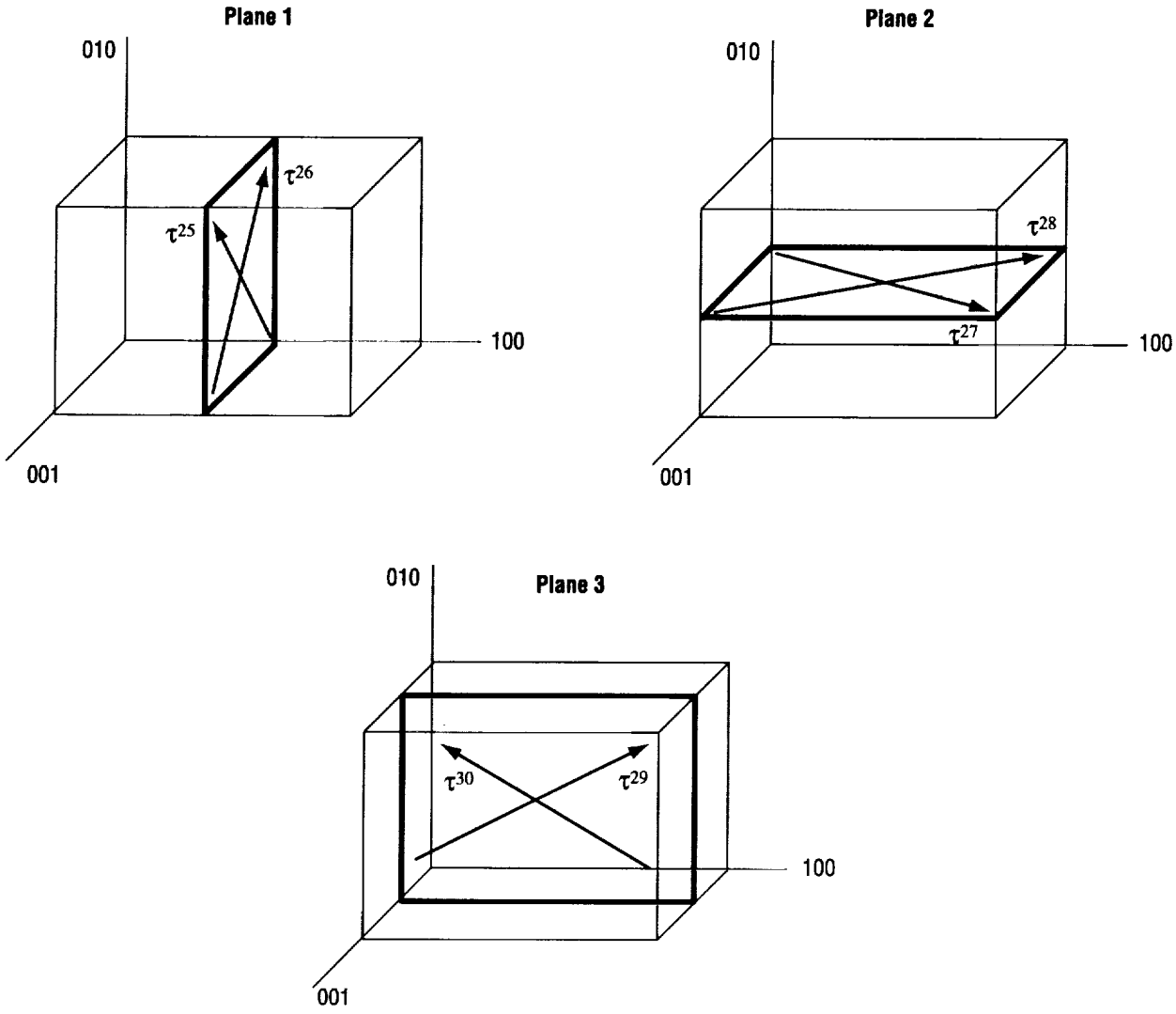

Figure 10. Cube slip planes and slip directions for an FCC crystal.[4]

Table 1. Slip planes and slip directions in an FCC crystal.[4]

Slip Number	Slip Plane	Slip Direction
	Octahedral Slip a/2<110>{111}	12 Primary Slip Directions
1	[1 1 1]	[1 0 −1]
2	[1 1 1]	[0 −1 1]
3	[1 1 1]	[1 −1 0]
4	[−1 1 −1]	[1 0 −1]
5	[−1 1 −1]	[1 1 0]
6	[−1 1 −1]	[0 1 1]
7	[1 −1 −1]	[1 1 0]
8	[1 −1 −1]	[0 −1 1]
9	[1 −1 −1]	[1 0 1]
10	[−1 −1 1]	[0 1 1]
11	[−1 −1 1]	[1 0 1]
12	[−1 −1 1]	[1 −1 0]
	Octahedral Slip a/2<112>{111}	12 Secondary Slip Directions
13	[1 1 1]	[−1 2 −1]
14	[1 1 1]	[2 −1 −1]
15	[1 1 1]	[−1 −1 2]
16	[−1 1 −1]	[1 2 1]
17	[−1 1 −1]	[1 −1 −2]
18	[−1 1 −1]	[−2 −1 1]
19	[1 −1 −1]	[−1 1 −2]
20	[1 −1 −1]	[2 1 1]
21	[1 −1 −1]	[−1 −2 1]
22	[−1 −1 1]	[−2 1 −1]
23	[−1 −1 1]	[1 −2 −1]
24	[−1 −1 1]	[1 1 2]
	Cube Slip a/2<110>{100}	6 Cube Slip Directions
25	[1 0 0]	[0 1 1]
26	[1 0 0]	[0 1 −1]
27	[0 1 0]	[1 0 1]
28	[0 1 0]	[1 0 −1]
29	[0 0 1]	[1 1 0]
30	[0 0 1]	[−1 1 0]

3.3 Fatigue Crack Initiation

Crack initiation in PWA 1480 and 1484 fall into two broad classifications: crystallographic and noncrystallographic. Microstructural properties, environmental factors, and mechanical factors (stress intensity, loading, surface tractions, etc.) are all important factors that affect crack initiation. The macrostructure of single-crystal Ni superalloys is characterized by parallel, continuous primary dendrites spanning the casting in the direction of solidification (<001>). Secondary dendrite arms, perpendicular to solidification direction, define the interdendritic spacing. Microstructural discontinuities such as carbides, undissolved eutectic pools, and associated microporosity (point-source defects) are concentrated in the interdendritic regions and often exert a controlling influence on the fatigue crack initiation behavior of the alloy.[2] These discontinuities are aligned in long columns, paralleling the primary dendrites. They inhibit long-range dislocation motion and can act as crack initiation sites in the alloy microstructure. The interaction between the effects of environment, temperature, and stress intensity determines which particular point-source defect species initiates a crystallographic or noncrystallographic fatigue crack.[2] At low temperature and stress conditions, crystallographic initiation appears to be the most prevalent mode. This mode warrants special consideration since this mode of cracking has been observed in many turbine blade failures.

3.3.1 Carbides

In room-temperature air, carbides typically initiate crystallographic fracture. The subsurface shear stresses induced by fretting action can result in crystallographic initiation of failure, as seen in figure 11, which shows a subsurface fatigue crack emanating from a tantalum and carbon (TaC) carbide in a turbine blade attachment (PWA 1422, a columnar grain Ni-based superalloy) and propagating along octahedral (111) planes.[2] TaC is a noncoherent defect, which rules out crystallographic shear, and suggests that the primary failure mechanism may be slip-band impingment.[2] Fretting fatigue at low slip amplitudes that induces little or no surface damage can result in greatly reduced fatigue life with accelerated subsurface crack initiation, akin to subsurface shear stress-induced, rolling bearing fatigue. A good example of this phenomena is seen in figure 12 which shows an underside view of a single-crystal (PWA 1493) turbine blade platform tip fretting failure at the contact where a centrifugal damper impinged the blade platform.[6] The damper was subjected to an alternating compressive load, generating subsurface shear stresses similar to rolling contact. The fretting fatigue crack initiation was clearly subsurface, propagating along intersecting (111) crystallographic planes until breaking out to the surface. The piece was subsequently ejected. An identical scenario occurred with the impinging damper. The damper was quite small and cast in a very coarse grained form such that the contact point was a single large grain. It too exhibited a subsurface crystallographic shear fatigue crack initiation/propagation on multiple intersecting octahedral planes leading to a pyramidal "hole" in the component as the "chip" was ejected. To summarize, in room-temperature air, carbides are favored over pores or eutectics. At moderately high temperature (>593 °C) initiation at TaC carbides predominates over occasional (111) eutectic origins. In the presence of porosity, TaC and pores are frequently in intimate contact and it is difficult to differentiate between the TaC and micropore initiation.

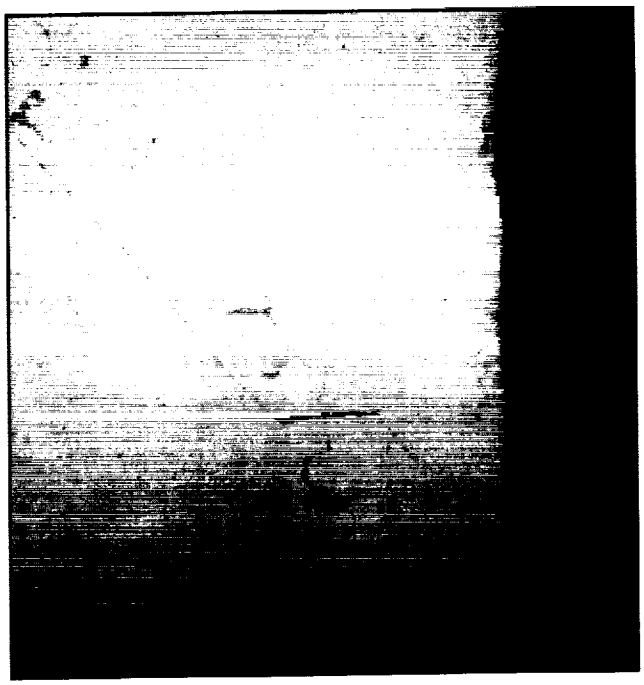

× 320

Figure 11. A subsurface fretting fatigue crack emanating from a carbide in a turbine blade attachment (PWA 1422) and propagating along octahedral (111) shear planes.[1]

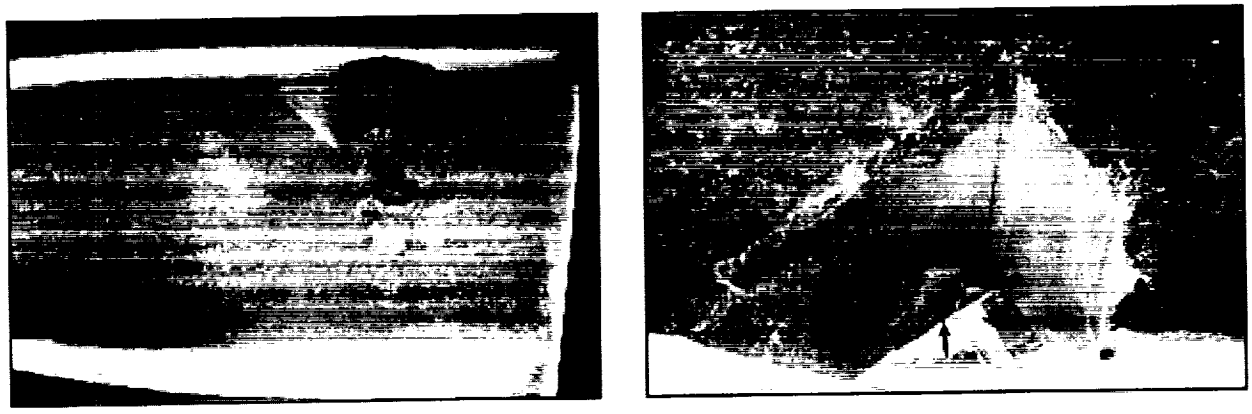

Figure 12. Subsurface fretting fatigue crystallographic crack initiation in a single-crystal Ni turbine blade platform.[5]

3.3.2 Microporosity

Perhaps the most frequently observed fatigue crack initiator in LCF and HCF specimen testing of PWA 1480 and non-hot isostatic pressing (HIP) PWA 1484 is microporosity. Porosity can be eliminated in some cases by HIP. Fatigue cracks frequently originate at microporosity when tested in air at moderate temperature (>427 °C (800 °F)). In room-temperature air (26 °C (79 °F)), fatigue crack initiation switches from microporosity to small carbides. For non-HIP microstructures at moderately high temperature (>593 °C (1,100 °F)), it is difficult to differentiate between the TaC and micropore initiation, since they are generally in intimate contact.[2]

3.3.3 Eutectic Micromechanisms

The eutectic γ/γ' are elementally and structurally different from the surrounding γ/γ' regions and can act as crack initiation sites. The eutectic phase can initiate fatigue cracks by three different micromechanisms, depending on the operating conditions. At room temperature (26 °C (79 °F)), in high-pressure hydrogen, the eutectic γ/γ' initiates fatigue cracks by an interlaminar (between γ and γ') failure mechanism.[7] This failure mechanism typically exhibits cracking in the <001> family of directions since the eutectic is coherent with the microstructure and the γ/γ' interfaces lie parallel to the (001) planes, resulting in cracking in multiple "cubic" directions. At intermediate temperatures (250–427 °C (482–800 °F)) in air, the eutectic can initiate noncrystallographic fracture by a disbonding mechanism.[2] At moderately high temperature (>593 °C (1,100 °F)), dislocation shearing of the eutectic is also possible, since it is coherent with the microstructure, leading to a crystallographic (111) fatigue crack initiation by eutectic cleavage.[2] This condition is true for HIP microstructures.

To summarize, the eutectic becomes the operative defect in the presence of hydrogen by an interlaminar failure mechanism. At intermediate temperature in air, the eutectic is operative but failure is by a disbonding mechanism leading to noncrystallographic crack initiation. At moderately high-temperature, initiation at TaC carbides predominates over occasional (111) eutectic origins. These three failure mechanisms illustrate the complex crack initiation behavior exhibited by the eutectic under a variety of temperature and environmental conditions.

3.4 Fatigue Crack Growth Behavior

The fatigue crack growth (FCG) behavior of single-crystal Ni superalloys is governed by a complex interaction between the operative deformation mechanism, stress intensity, and environmental conditions. The operative deformation mechanism has a strong influence on the nature of fracture. From a standpoint of energy balance, the formation of a crack or free surface results from the application of strain energy in the cyclic plastic zone ahead of the crack tip. One of the ways the increasing amounts of strain energy being input to the system during the fatigue process is dissipated is by the creation of additional amounts of free surface. Fracture or free surface development is aided by dislocation exhaustion on crystallographic planes in the critical zone.[2] When lattice plane dislocation densities reach critical values, cohesive forces are weakened; hence, the fracture assumes the character of the deformation mechanism.

The FCG behavior is determined by the operative microscopic fracture mode. As a result of the two-phase microstructure present in single-crystal Ni alloys, a complex set of fracture mode exists based on the dislocation motion in the matrix (γ) and precipitate phase (γ'). Telesman and Ghosn[8] have observed

the transition of fracture mode as a function of stress intensity (K) in PWA 1480 at room temperature. They identified that fatigue failure along (111) planes (ΔK>8 MPa $m^{1/2}$) is associated with the Paris region crack growth behavior, while failure along (001) planes (ΔK<8 MPa $m^{1/2}$) was associated with the accelerated FCG behavior at low ΔK_{rss}. They also noted that K_{rss}, the resolved shear stress intensity parameter on the 12 primary slip planes, predicted the crack zig-zag behavior caused by fracture mode transitions. Deluca and Cowles[7] have observed the fracture mode transition that is environmentally dependent (presence of high-pressure hydrogen), explained in eutectic micromechanisms.

Failure on the (111) octahedral slip planes is governed by the resolved shear stresses and not the maximum principal stresses. However stresses normal to the plane (mode I component) are thought to play some role in the failure process.[9] The importance of normal stress is based on the observations of the crack tip remaining open for cracks growing on octahedral planes, and the presence of cleavage-type features on the fracture surfaces, for a variety of loading conditions or R values. Crack growth on the (111) slip planes at an oblique angle to the loading direction was observed at lower temperatures (427–593 °C) and higher frequencies, while a mode I crack growth perpendicular to the loading direction was observed at higher temperatures (760–871 °C) and lower frequencies.[9]

Crystallographic crack growth along (111) planes under mixed mode loading can be an order of magnitude faster than under pure mode I loading.[10] This increase in crack growth rate implies that any damage tolerance-based design using only mode I data can lead to overestimation of crack growth life when actual service conditions produce mixed mode loading along a potential failure plane (e.g., at blade attachment surfaces). These results have important implications on fretting fatigue. Since fretting action results in mixed mode loading, this can result in crystallographic initiation along (111) slip planes and rapid crack growth under loads lower than that expected under mode I loading. Crystallographic subsurface crack initiation induced by fretting action at a single-crystal (PWA 1422) turbine blade attachment region is shown in figure 11.

3.5 Adaptation of Fatigue Failure Criteria for Polycrystalline Material to Single-Crystal Material

Fatigue life estimation of single-crystal turbine blade components represents an important aspect of durability assessment. Towards identifying a fatigue failure criteria for single-crystal material, some failure criteria used for polycrystalline material subjected to multiaxial states of fatigue stress are outlined first. Plausible fatigue failure criteria for single crystals are proposed, based on the combination of failure theories for polycrystalline material with the models for deformation mechanisms and crack initiation properties for single crystals outlined earlier.

Turbine blade material is subjected to large mean stresses from the centrifugal stress field. High-frequency, alternating fatigue stresses are a function of the vibratory characteristics of the blade. Any fatigue failure criteria chosen must have the ability to account for high mean stress effects. The LCF regime is characterized by crack formation and growth that is governed by the maximum shear strain amplitude. The maximum shear stress theory modified by the influence of the complementary normal stress is considered an effective theory for multiaxial fatigue.[11] Kandil et al.[12] presented a shear and normal strain-based model, shown in equation (1), based on the critical plane approach which postulates that cracks initiate and grow on certain planes and that the normal strains to those planes assist in the fatigue crack growth process.

In equation (1) γ_{max} is the maximum shear strain on the critical plane, ε_n the normal strain on the same plane, S is a constant, and N is the cycles to initiation:

$$\gamma_{max} + S\varepsilon_n = f(N) \quad . \tag{1}$$

Socie et al.[13] presented a modified version of this theory, shown in equation (2), to include mean stress effects:

$$\frac{\Delta\gamma}{2} + \frac{\Delta\varepsilon_n}{2} + \frac{\sigma_{no}}{E} = f(N) \quad . \tag{2}$$

Here the maximum shear strain amplitude ($\Delta\gamma$) is modified by the normal strain amplitude ($\Delta\varepsilon$) and the mean stress normal to the maximum shear strain amplitude (σ_{no}). The modifications are incorporated to account for observed changes in crack closure for different stress/strain states. These observations are similar to FCG on octahedral planes for single crystals, explained in the previous section.

Fatemi and Socie[14] have presented an alternate shear-based model for multiaxial mean/stress loadings that exhibit substantial out-of-phase hardening, shown in equation (3):

$$\frac{\Delta\gamma}{2}\left(1 + k\frac{\sigma_n^{max}}{\sigma_y}\right) = f(N) \quad . \tag{3}$$

The modifying parameter here is the maximum stress normal to the maximum shear strain amplitude. This model indicates that no shear direction crack growth occurs if there is no shear alternation.

Smith et al.[15] proposed a uniaxial parameter to account for mean stress effects which was modified for multiaxial loadings, shown in equation (4), by Bannantine and Socie.[16]

$$\frac{\Delta\varepsilon_1}{2}\left(\sigma^{max}\right) = f(N) \quad . \tag{4}$$

Here the maximum principal strain amplitude is modified by the maximum stress in the direction of maximum principal strain amplitude that occurs over one cycle.

The polycrystalline failure parameters based on the critical plane approach will be applied for single-crystal uniaxial LCF test data. The failure parameters will be evaluated on all of the 30 slip systems. For instance, in equation (1), γ_{max} will be the maximum value of shear strain computed on the 30 slip systems, and ε_n will be the normal strain on the slip system where the shear strain is maximum. The composite failure parameters evaluated on the slip systems will be plotted against cycles to failure. The widely used yield criteria for ductile polycrystalline materials, based on Von Mises and Tresca theories, will also be used as failure parameters to represent the LCF test data. The parameter that collapses the LCF data with the best power law fit will be chosen as the failure parameter. Application of the proposed failure parameters to LCF data is explained in section 4.

4. APPLICATION OF FAILURE CRITERIA FOR LCF TEST DATA

4.1 Introduction

This section outlines the application of failure criteria proposed in section 3 for uniaxial LCF test data. Uniaxial fatigue test data are well suited for testing the efficacy of the proposed failure criteria because closed-form expressions for shear and normal stresses and strains on the 24 octahedral and 6 cube slip systems can be computed readily. This feature greatly facilitates computation of the various composite failure criteria proposed and selection of the most effective parameter that fits the test data. A useful fatigue life equation is obtained based on the curve fit of the failure parameter with LCF test data.

4.2 Coordinate Transformations for Orthotropic Material

Transformation of the stress and strain tensors between the material and specimen coordinate systems is necessary for implementing the failure theories outlined. We now describe relations necessary for transforming stresses and strains between the material coordinate system (x, y, z), and the specimen coordinate system (x', y', z'), as shown in figure 13. These transformations are based on the derivations by Lekhnitskii.[17] The position of the (x, y, z) system with respect to the (x', y', z') system is determined by direction cosines shown in table 2. The components of stresses in the (x', y', z') system in terms of the (x, y, z) system is given by

$$\{\sigma'\} = [\mathbf{Q}']\{\sigma\} \tag{5}$$

$$\{\sigma\} = [\mathbf{Q}']^{-1}\{\sigma'\} = [\mathbf{Q}]\{\sigma'\} \ , \tag{6}$$

where

$$\{\sigma'\} = \begin{Bmatrix} \sigma'_x \\ \sigma'_y \\ \sigma'_z \\ \tau'_{yz} \\ \tau'_{zx} \\ \tau'_{xy} \end{Bmatrix} \quad \text{and} \quad \{\sigma\} = \begin{Bmatrix} \sigma_x \\ \sigma_y \\ \sigma_z \\ \tau_{yz} \\ \tau_{zx} \\ \tau_{xy} \end{Bmatrix} \tag{7}$$

and

$$[\mathbf{Q}] = \begin{bmatrix} \alpha_1^2 & \alpha_2^2 & \alpha_3^2 & 2\alpha_3\alpha_2 & 2\alpha_1\alpha_3 & 2\alpha_2\alpha_1 \\ \beta_1^2 & \beta_2^2 & \beta_3^2 & 2\beta_3\beta_2 & 2\beta_1\beta_3 & 2\beta_2\beta_1 \\ \gamma_1^2 & \gamma_2^2 & \gamma_3^2 & 2\gamma_3\gamma_2 & 2\gamma_1\gamma_3 & 2\gamma_2\gamma_1 \\ \beta_1\gamma_1 & \beta_2\gamma_2 & \beta_3\gamma_3 & (\beta_2\gamma_3 + \beta_3\gamma_2) & (\beta_1\gamma_3 + \beta_3\gamma_1) & (\beta_1\gamma_2 + \beta_2\gamma_1) \\ \gamma_1\alpha_1 & \gamma_2\alpha_2 & \gamma_3\alpha_3 & (\gamma_2\alpha_3 + \gamma_3\alpha_2) & (\gamma_1\alpha_3 + \gamma_3\alpha_1) & (\gamma_1\alpha_2 + \gamma_2\alpha_1) \\ \alpha_1\beta_1 & \alpha_2\beta_2 & \alpha_3\beta_3 & (\alpha_2\beta_3 + \alpha_3\beta_2) & (\alpha_1\beta_3 + \alpha_3\beta_1) & (\alpha_1\beta_2 + \alpha_2\beta_1) \end{bmatrix} . \quad (8)$$

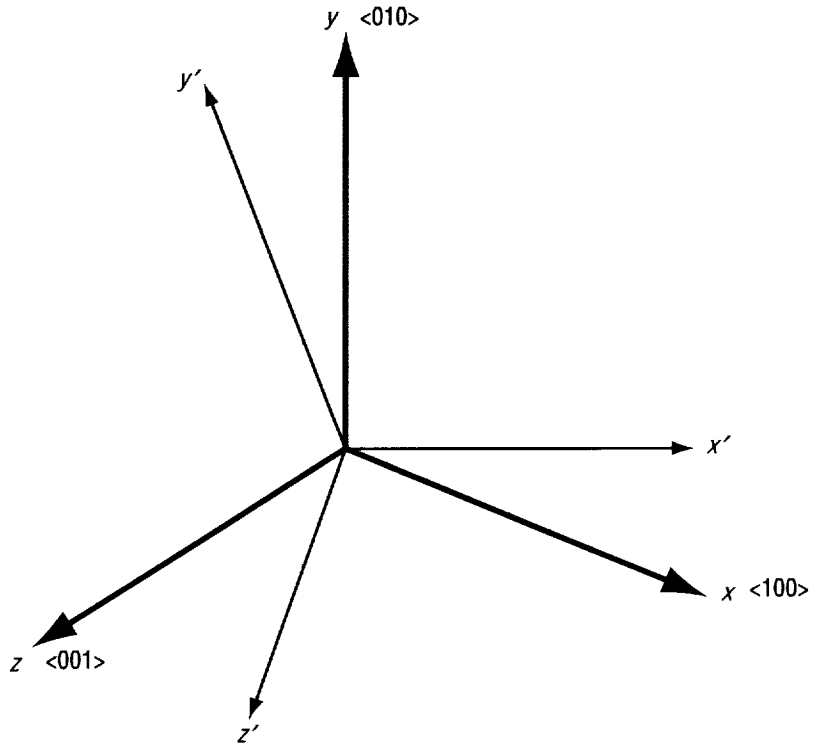

Figure 13. Material (x, y, z) and specimen (x', y', z') coordinate systems.

Table 2. Direction cosines.

	x	y	z
x′	α_1	β_1	γ_1
y′	α_2	β_2	γ_2
z′	α_3	β_3	γ_3

The transformation matrix [**Q**] is orthogonal and hence $[\mathbf{Q}]^{-1} = [\mathbf{Q}]^{T} = [\mathbf{Q}']$. The strain vector transformation matrix is different from [**Q**] because $\gamma xy = 2\varepsilon xy$, $\gamma_{zx} = 2\varepsilon_{zx}$, and $\gamma_{yz} = 2\varepsilon_{yz}$, which accounts for engineering versus tensor shear strain components.

$$\begin{aligned} \{\varepsilon'\} &= [\mathbf{Q}'_{\varepsilon}]\{\varepsilon\} \\ \{\varepsilon\} &= [\mathbf{Q}'_{\varepsilon}]^{-1}\{\varepsilon'\} = [\mathbf{Q}_{\varepsilon}]\{\varepsilon'\} \ , \end{aligned} \tag{9}$$

where

$$\{\boldsymbol{\varepsilon}'\} = \begin{Bmatrix} \varepsilon'_x \\ \varepsilon'_y \\ \varepsilon'_z \\ \gamma'_{yz} \\ \gamma'_{zx} \\ \gamma'_{xy} \end{Bmatrix} \text{ and } \{\boldsymbol{\varepsilon}\} = \begin{Bmatrix} \varepsilon_x \\ \varepsilon_y \\ \varepsilon_z \\ \gamma_{yz} \\ \gamma_{zx} \\ \gamma_{xy} \end{Bmatrix} \tag{10}$$

and

$$[\mathbf{Q}_{\varepsilon}] = \begin{bmatrix} \alpha_1^2 & \alpha_2^2 & \alpha_3^2 & \alpha_3\alpha_2 & \alpha_1\alpha_3 & \alpha_2\alpha_1 \\ \beta_1^2 & \beta_2^2 & \beta_3^2 & \beta_3\beta_2 & \beta_1\beta_3 & \beta_2\beta_1 \\ \gamma_1^2 & \gamma_2^2 & \gamma_3^2 & \gamma_3\gamma_2 & \gamma_1\gamma_3 & \gamma_2\gamma_1 \\ 2\beta_1\gamma_1 & 2\beta_2\gamma_2 & 2\beta_3\gamma_3 & (\beta_2\gamma_3+\beta_3\gamma_2) & (\beta_1\gamma_3+\beta_3\gamma_1) & (\beta_1\gamma_2+\beta_2\gamma_1) \\ 2\gamma_1\alpha_1 & 2\gamma_2\alpha_2 & 2\gamma_3\alpha_3 & (\gamma_2\alpha_3+\gamma_3\alpha_2) & (\gamma_1\alpha_3+\gamma_3\alpha_1) & (\gamma_1\alpha_2+\gamma_2\alpha_1) \\ 2\alpha_1\beta_1 & 2\alpha_2\beta_2 & 2\alpha_3\beta_3 & (\alpha_2\beta_3+\alpha_3\beta_2) & (\alpha_1\beta_3+\alpha_3\beta_1) & (\alpha_1\beta_2+\alpha_2\beta_1) \end{bmatrix} . \tag{11}$$

The generalized Hooke's law for a homogeneous anisotropic body in Cartesian coordinates (x, y, z) is given below:[17]

$$\{\varepsilon\} = [a_{ij}]\{\sigma\} \ , \tag{12}$$

where $[\mathbf{a}_{ij}]$ is the matrix of 36 elastic coefficients, of which only 21 are independent, since $[a_{ij}] = [a_{ji}]$. An equivalent form of the generalized Hooke's law is

$$\{\boldsymbol{\sigma}\} = [A_{ij}]\{\boldsymbol{\varepsilon}\} \ , \tag{13}$$

where $[A_{ij}] = [a_{ij}]^{-1}$ is the matrix of elastic moduli.

The elastic properties of FCC crystals exhibit cubic symmetry, also described as cubic syngony. Materials with cubic symmetry have only three independent elastic constants designated as the elastic modulus, shear modulus, and Poisson ratio.[4] Invoking the rules of elastic symmetry for a material exhibiting cubic syngony,[17] we see that $[a_{ij}]$ has only three independent elastic constants, as given below:

$$[a_{ij}] = \begin{bmatrix} a_{11} & a_{12} & a_{12} & 0 & 0 & 0 \\ a_{12} & a_{11} & a_{12} & 0 & 0 & 0 \\ a_{12} & a_{12} & a_{11} & 0 & 0 & 0 \\ 0 & 0 & 0 & a_{44} & 0 & 0 \\ 0 & 0 & 0 & 0 & a_{44} & 0 \\ 0 & 0 & 0 & 0 & 0 & a_{44} \end{bmatrix} . \tag{14}$$

The elastic constants are defined as

$$a_{11} = \frac{1}{E_{xx}},\ a_{44} = \frac{1}{G_{yz}},\ a_{12} = -\frac{\nu_{yx}}{E_{xx}} = -\frac{\nu_{xy}}{E_{yy}} . \tag{15}$$

Unlike for isotropic materials, the components of $[a_{ij}]$ are a function of orientation. Equation (12) is valid only when the loading is in the principal direction of the material or parallel to the edges of the FCC lattice.

4.2.1 The Transformation of Elastic Constants Under a Coordinate System Transformation

The elastic constants in the generalized Hooke's law of an anisotropic body, defined by the matrix $[a_{ij}]$, vary with the direction of the coordinate axes. In the case of an isotropic body, the constants are invariant in any orthogonal coordinate system. Transformation of second-order tensors under a coordinate system transformation is described in detail by Lekhnitskii[17] and only the final results are presented here.

The Hooke's law in the (x, y, z) coordinate system is given by equation (12): $\{\varepsilon\} = [a_{ij}]\{\sigma\}$. Our objective is to find the elastic constant matrix $[a'_{ij}]$ in the (x', y', z') coordinate system that relates $\{\varepsilon'\}$ and $\{\sigma'\}$, as in equation (16):

$$\{\varepsilon'\} = [a'_{ij}]\{\sigma'\} . \tag{16}$$

The elastic constant matrix transforms as follows, under a coordinate transformation:

$$\left[a'_{ij}\right] = [Q]^T \left[a_{ij}\right] [Q] = \sum_{m=1}^{6} \sum_{n=1}^{6} a_{mn} Q_{mi} Q_{nj} \qquad (i, j = 1, 2, \ldots, 6) \quad . \tag{17}$$

We can now transform the elastic constants and hence the stresses and strains between the material coordinate system (x, y, z) and the specimen coordinate system (x', y', z').

4.2.2 Shear Stresses and Strains on the Crystallographic Slip Systems

Knowing the stresses and strains in the material coordinate system (x, y, z), we can compute the shear stress and strain components on octahedral and cube planes, using the appropriate kinematic relations.[4] Table 1 shows the 30 slip systems possible in an FCC crystal. Shear stresses in the 30 slip systems are denoted by τ^1, τ^2, ..., τ^{30}. The shear stresses on the 12 primary octahedral slip directions are

$$\begin{Bmatrix} \tau^1 \\ \tau^2 \\ \tau^3 \\ \tau^4 \\ \tau^5 \\ \tau^6 \\ \tau^7 \\ \tau^8 \\ \tau^9 \\ \tau^{10} \\ \tau^{11} \\ \tau^{12} \end{Bmatrix} = \frac{1}{\sqrt{6}} \begin{bmatrix} 1 & 0 & -1 & 1 & 0 & -1 \\ 0 & -1 & 1 & -1 & 1 & 0 \\ 1 & -1 & 0 & 0 & 1 & -1 \\ -1 & 0 & 1 & 1 & 0 & -1 \\ -1 & 1 & 0 & 0 & -1 & -1 \\ 0 & 1 & -1 & -1 & -1 & 0 \\ 1 & -1 & 0 & 0 & -1 & -1 \\ 0 & 1 & -1 & -1 & 1 & 0 \\ 1 & 0 & -1 & -1 & 0 & -1 \\ 0 & -1 & 1 & -1 & -1 & 0 \\ -1 & 0 & 1 & -1 & 0 & -1 \\ -1 & 1 & 0 & 0 & 1 & -1 \end{bmatrix} \begin{Bmatrix} \sigma_{xx} \\ \sigma_{yy} \\ \sigma_{zz} \\ \sigma_{xy} \\ \sigma_{zx} \\ \sigma_{yz} \end{Bmatrix} . \tag{18}$$

Shear stresses on the 12 secondary octahedral slip planes are given by

$$\begin{Bmatrix} \tau^{13} \\ \tau^{14} \\ \tau^{15} \\ \tau^{16} \\ \tau^{17} \\ \tau^{18} \\ \tau^{19} \\ \tau^{20} \\ \tau^{21} \\ \tau^{22} \\ \tau^{23} \\ \tau^{24} \end{Bmatrix} = \frac{1}{3\sqrt{2}} \begin{bmatrix} -1 & 2 & -1 & 1 & -2 & 1 \\ 2 & -1 & -1 & 1 & 1 & -2 \\ -1 & -1 & 2 & -2 & 1 & 1 \\ -1 & 2 & -1 & -1 & -2 & -1 \\ -1 & -1 & 2 & 2 & 1 & -1 \\ 2 & -1 & -1 & -1 & 1 & 2 \\ -1 & -1 & 2 & 2 & -1 & 1 \\ 2 & -1 & -1 & -1 & -1 & -2 \\ -1 & 2 & -1 & -1 & 2 & 1 \\ 2 & -1 & -1 & 1 & -1 & 2 \\ -1 & 2 & -1 & 1 & 2 & -1 \\ -1 & -1 & 2 & -2 & -1 & -1 \end{bmatrix} \begin{Bmatrix} \sigma_{xx} \\ \sigma_{yy} \\ \sigma_{zz} \\ \sigma_{xy} \\ \sigma_{zx} \\ \sigma_{yz} \end{Bmatrix} , \tag{19}$$

and the shear stresses on the six cube slip systems are

$$\begin{Bmatrix} \tau^{25} \\ \tau^{26} \\ \tau^{27} \\ \tau^{28} \\ \tau^{29} \\ \tau^{30} \end{Bmatrix} = \frac{1}{\sqrt{2}} \begin{bmatrix} 0 & 0 & 0 & 1 & 1 & 0 \\ 0 & 0 & 0 & 1 & -1 & 0 \\ 0 & 0 & 0 & 1 & 0 & 1 \\ 0 & 0 & 0 & 1 & 0 & -1 \\ 0 & 0 & 0 & 0 & 1 & 1 \\ 0 & 0 & 0 & 0 & -1 & 1 \end{bmatrix} \begin{Bmatrix} \sigma_{xx} \\ \sigma_{yy} \\ \sigma_{zz} \\ \sigma_{xy} \\ \sigma_{zx} \\ \sigma_{yz} \end{Bmatrix}. \tag{20}$$

Shear strains (engineering) on the 30 slip systems are calculated using equations (21)–(23):

$$\begin{Bmatrix} \gamma^{1} \\ \gamma^{2} \\ \gamma^{3} \\ \gamma^{4} \\ \gamma^{5} \\ \gamma^{6} \\ \gamma^{7} \\ \gamma^{8} \\ \gamma^{9} \\ \gamma^{10} \\ \gamma^{11} \\ \gamma^{12} \end{Bmatrix} = \frac{2}{\sqrt{6}} \begin{bmatrix} 1 & 0 & -1 & 1 & 0 & -1 \\ 0 & -1 & 1 & -1 & 1 & 0 \\ 1 & -1 & 0 & 0 & 1 & -1 \\ -1 & 0 & 1 & 1 & 0 & -1 \\ -1 & 1 & 0 & 0 & -1 & -1 \\ 0 & 1 & -1 & -1 & -1 & 0 \\ 1 & -1 & 0 & 0 & -1 & -1 \\ 0 & 1 & -1 & -1 & 1 & 0 \\ 1 & 0 & -1 & -1 & 0 & -1 \\ 0 & -1 & 1 & -1 & -1 & 0 \\ -1 & 0 & 1 & -1 & 0 & -1 \\ -1 & 1 & 0 & 0 & 1 & -1 \end{bmatrix} \begin{Bmatrix} \varepsilon_{xx} \\ \varepsilon_{yy} \\ \varepsilon_{zz} \\ \varepsilon_{xy} \\ \varepsilon_{zx} \\ \varepsilon_{yz} \end{Bmatrix} \tag{21}$$

$$\begin{Bmatrix} \gamma^{13} \\ \gamma^{14} \\ \gamma^{15} \\ \gamma^{16} \\ \gamma^{17} \\ \gamma^{18} \\ \gamma^{19} \\ \gamma^{20} \\ \gamma^{21} \\ \gamma^{22} \\ \gamma^{23} \\ \gamma^{24} \end{Bmatrix} = \frac{2}{3\sqrt{2}} \begin{bmatrix} -1 & 2 & -1 & 1 & -2 & 1 \\ 2 & -1 & -1 & 1 & 1 & -2 \\ -1 & -1 & 2 & -2 & 1 & 1 \\ -1 & 2 & -1 & -1 & -2 & -1 \\ -1 & -1 & 2 & 2 & 1 & -1 \\ 2 & -1 & -1 & -1 & 1 & 2 \\ -1 & -1 & 2 & 2 & -1 & 1 \\ 2 & -1 & -1 & -1 & -1 & -2 \\ -1 & 2 & -1 & -1 & 2 & 1 \\ 2 & -1 & -1 & 1 & -1 & 2 \\ -1 & 2 & -1 & 1 & 2 & -1 \\ -1 & -1 & 2 & -2 & -1 & -1 \end{bmatrix} \begin{Bmatrix} \varepsilon_{xx} \\ \varepsilon_{yy} \\ \varepsilon_{zz} \\ \varepsilon_{xy} \\ \varepsilon_{zx} \\ \varepsilon_{yz} \end{Bmatrix} \tag{22}$$

$$\begin{Bmatrix} \gamma^{25} \\ \gamma^{26} \\ \gamma^{27} \\ \gamma^{28} \\ \gamma^{29} \\ \gamma^{30} \end{Bmatrix} = \frac{2}{\sqrt{2}} \begin{bmatrix} 0 & 0 & 0 & 1 & 1 & 0 \\ 0 & 0 & 0 & 1 & -1 & 0 \\ 0 & 0 & 0 & 1 & 0 & 1 \\ 0 & 0 & 0 & 1 & 0 & -1 \\ 0 & 0 & 0 & 0 & 1 & 1 \\ 0 & 0 & 0 & 0 & -1 & 1 \end{bmatrix} \begin{Bmatrix} \varepsilon_{xx} \\ \varepsilon_{yy} \\ \varepsilon_{zz} \\ \varepsilon_{xy} \\ \varepsilon_{zx} \\ \varepsilon_{yz} \end{Bmatrix} . \tag{23}$$

4.2.3 Example Problem: Applied Uniaxial Stress (Load Control)

We consider a uniaxial test specimen loaded in the [110] direction, which is chosen as the x' axis, as shown in figure 14. An arbitrary stress value of 1,000 psi is applied along the x' axis; i.e., in the direction [110]. We wish to calculate the resolved shear stress in each of the 30 slip planes for an FCC crystal. Since we know the stress $\{\sigma'\}$ in the specimen coordinate system (x', y', z'), we need to calculate the stress $\{\sigma\}$ in the material coordinate system (x, y, z). From equation (6) we have $\{\sigma\} = [\mathbf{Q}']^{-1}\{\sigma'\} = [\mathbf{Q}]\{\sigma'\}$.

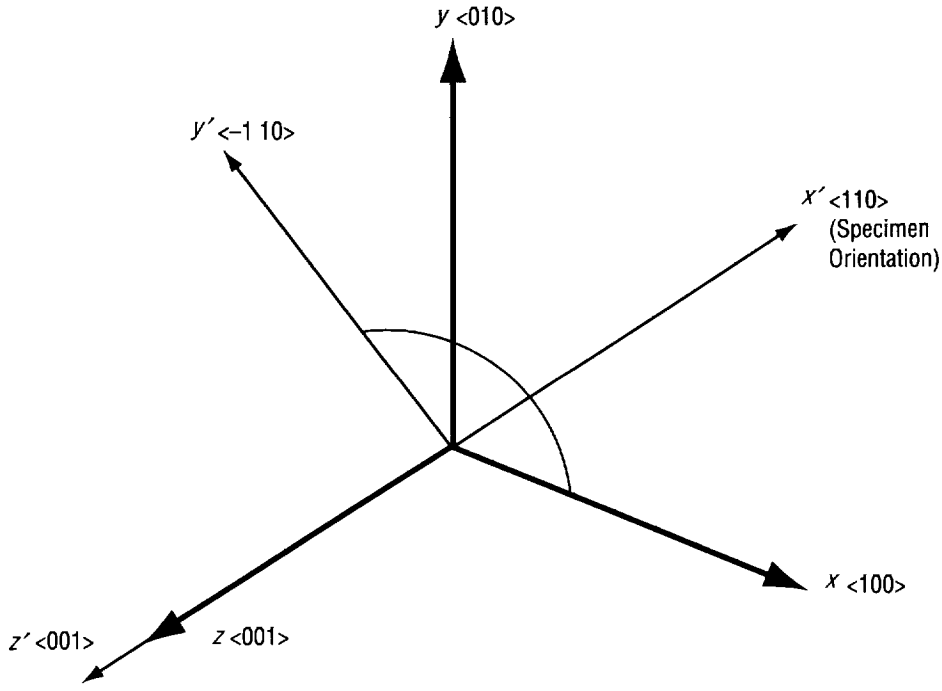

Figure 14. Specimen loaded in the [110] direction.

We need the direction cosines of (x', y', z') with respect to (x, y, z). We align the x' axis along the [110] direction and calculate the direction cosines shown in table 3.

Table 3. x' axis aligned with the [110] axis direction cosines.

	x	y	z
x'	α_1=0.707	β_1=0.707	γ_1=0
y'	α_2=–0.707	β_2=0.707	γ_2=0
z'	α_3=0	β_3=0	γ_3=1

The [**Q**] matrix is given by

$$[\mathbf{Q}]=\begin{bmatrix} 0.5 & 0.5 & 0 & 0 & 0 & -1 \\ 0.5 & 0.5 & 0 & 0 & 0 & 1 \\ 0 & 0 & 1 & 0 & 0 & 0 \\ 0 & 0 & 0 & 0.707 & 0.707 & 0 \\ 0 & 0 & 0 & -0.707 & 0.707 & 0 \\ 0.5 & -0.5 & 0 & 0 & 0 & 0 \end{bmatrix}. \tag{24}$$

Stresses in the material coordinate system (x, y, z), using equation (6), is calculated as

$$\begin{Bmatrix} \sigma_{xx} \\ \sigma_{yy} \\ \sigma_{zz} \\ \sigma_{xy} \\ \sigma_{zx} \\ \sigma_{yz} \end{Bmatrix} = [\mathbf{Q}] \begin{Bmatrix} 1{,}000 \\ 0 \\ 0 \\ 0 \\ 0 \\ 0 \end{Bmatrix} = \begin{Bmatrix} 500 \\ 500 \\ 0 \\ 500 \\ 0 \\ 0 \end{Bmatrix}. \tag{25}$$

Using equations (18)–(20), we obtain the shear stresses in the 30 slip systems as

$$\begin{Bmatrix} \tau^1 \\ \tau^2 \\ \tau^3 \\ \tau^4 \\ \tau^5 \\ \tau^6 \\ \tau^7 \\ \tau^8 \\ \tau^9 \\ \tau^{10} \\ \tau^{11} \\ \tau^{12} \end{Bmatrix} = \begin{Bmatrix} 408.25 \\ -408.25 \\ 0 \\ 0 \\ 0 \\ 0 \\ 0 \\ 0 \\ 0 \\ -408.25 \\ -408.25 \\ 0 \end{Bmatrix}, \begin{Bmatrix} \tau^{13} \\ \tau^{14} \\ \tau^{15} \\ \tau^{16} \\ \tau^{17} \\ \tau^{18} \\ \tau^{19} \\ \tau^{20} \\ \tau^{21} \\ \tau^{22} \\ \tau^{23} \\ \tau^{24} \end{Bmatrix} = \begin{Bmatrix} 235.70 \\ 235.70 \\ -471.40 \\ 0 \\ 0 \\ 0 \\ 0 \\ 0 \\ 0 \\ 235.70 \\ 235.70 \\ -471.40 \end{Bmatrix}, \begin{Bmatrix} \tau^{25} \\ \tau^{26} \\ \tau^{27} \\ \tau^{28} \\ \tau^{29} \\ \tau^{30} \end{Bmatrix} = \begin{Bmatrix} 353.55 \\ 353.55 \\ 353.55 \\ 353.55 \\ 0 \\ 0 \end{Bmatrix} . \tag{26}$$

The strain vector in the material coordinate system can be calculated using equations (12), (14), and (15). Using material property values of $\nu_{xy} = \nu_{yz} = \nu_{xz} = 0.4009$, $E = 1.54\text{E}07$ psi, and $G_{xy} = 1.57\text{E}07$ psi for PWA 1480 (or PWA 1493) at 1,200 °F, we have the $[a_{ij}]$ matrix as

$$[a_{ij}] = \begin{bmatrix} 6.494\text{E}-8 & -2.603\text{E}-8 & -2.603\text{E}-8 & 0 & 0 & 0 \\ -2.603\text{E}-8 & 6.494\text{E}-8 & -2.603\text{E}-8 & 0 & 0 & 0 \\ -2.603\text{E}-8 & -2.603\text{E}-8 & 6.494\text{E}-8 & 0 & 0 & 0 \\ 0 & 0 & 0 & 6.369\text{E}-8 & 0 & 0 \\ 0 & 0 & 0 & 0 & 6.369\text{E}-8 & 0 \\ 0 & 0 & 0 & 0 & 0 & 6.369\text{E}-8 \end{bmatrix} . \tag{27}$$

The strain vector in the material coordinate system, using equation (12), is

$$\begin{Bmatrix} \varepsilon_x \\ \varepsilon_y \\ \varepsilon_z \\ \gamma_{yz} \\ \gamma_{zx} \\ \gamma_{xy} \end{Bmatrix} = \begin{Bmatrix} 1.945\text{E}-5 \\ 1.945\text{E}-5 \\ -2.603\text{E}-5 \\ 3.185\text{E}-5 \\ 0 \\ 0 \end{Bmatrix} . \tag{28}$$

Shear strains on the slip systems can be computed using equations (21)–(23).

4.2.4 Example Problem: Applied Uniaxial Strain (Strain Control)

We consider a uniaxial test specimen loaded in the [213] direction (chosen as the x' axis) under strain control. The applied strain for the specimen is 1.212 percent. We wish to calculate the stress and strain vectors in the material coordinate system and the shear stresses on the 30 slip planes. We need the direction cosines of (x', y', z') with respect to (x, y, z). We align the x' axis along the [213] direction and calculate the direction cosines as shown in table 4.

Table 4. x' axis aligned with the [213] axis direction cosines

	x	y	z
x'	α_1=0.5445	β_1=0.2673	γ_1=0.8018
y'	α_2=−0.8320	β_2=0.0	γ_2=0.5547
z'	α_3=0.1482	β_3=−0.9636	γ_3=0.2223

We use equation (16) to calculate $\boldsymbol{\sigma}'_x$ in the specimen coordinate system $\{\varepsilon'\} = [a'_{ij}]\{\sigma'\}$.

The $[a'_{ij}]$ matrix is calculated using equation (17) as

$$[a'_{ij}] = \begin{bmatrix} 3.537\text{E}-8 & -2.644\text{E}-9 & -1.986\text{E}-8 & 5.209\text{E}-9 & 1.405\text{E}-8 & 1.878\text{E}-8 \\ -2.644\text{E}-9 & 3.975\text{E}-8 & -2.423\text{E}-8 & -5.61\text{E}-9 & 1.297\text{E}-8 & -2.023\text{E}-8 \\ -1.986\text{E}-8 & -2.423\text{E}-8 & 5.696\text{E}-8 & 4.007\text{E}-10 & -2.703\text{E}-8 & 1.445\text{E}-9 \\ 5.209\text{E}-9 & -5.61\text{E}-9 & 4.007\text{E}-10 & 7.089\text{E}-8 & 2.889\text{E}-9 & 2.595\text{E}-8 \\ 1.405\text{E}-8 & 1.297\text{E}-8 & -2.703\text{E}-8 & 2.889\text{E}-9 & 8.838\text{E}-8 & 1.042\text{E}-8 \\ 1.878\text{E}-8 & -2.023\text{E}-8 & 1.445\text{E}-9 & 2.595\text{E}-8 & 1.042\text{E}-8 & 1.572\text{E}-7 \end{bmatrix} . \quad (29)$$

Since $\boldsymbol{\sigma}'_x$ is the only nonzero stress in the specimen coordinate system, we see that

$$\sigma'_x = \frac{\varepsilon'_x}{a'_{11}} = \frac{0.01212}{3.537\text{E}-8} = 342{,}663 \text{ psi} . \quad (30)$$

Knowing $\{\boldsymbol{\sigma}'\}$, we can now calculate $\{\boldsymbol{\varepsilon}'\}$ as

$$\{\varepsilon'\} = \begin{Bmatrix} \varepsilon'_x \\ \varepsilon'_y \\ \varepsilon'_z \\ \gamma'_{yz} \\ \gamma'_{zx} \\ \gamma'_{xy} \end{Bmatrix} = [a'_{ij}] \begin{Bmatrix} 342{,}663 \\ 0 \\ 0 \\ 0 \\ 0 \\ 0 \end{Bmatrix} = \begin{Bmatrix} 0.01212 \\ -9.059\text{E}-4 \\ -6.805\text{E}-3 \\ 1.785\text{E}-3 \\ 4.815\text{E}-3 \\ 6.435\text{E}-3 \end{Bmatrix} . \quad (31)$$

The stresses in the material coordinate system can be calculated using either equation (6): $\{\sigma\} = [\mathbf{Q}']^{-1}\{\sigma'\} = [\mathbf{Q}]\{\sigma'\}$ or equation (13): $\{\boldsymbol{\sigma}\} = [\boldsymbol{A}_{ij}]\{\boldsymbol{\varepsilon}\}$.

The strains in the material coordinate system can again be calculated using either equation (9): $\{\varepsilon\} = [\mathbf{Q}_\varepsilon]\{\varepsilon'\}$ or equation (12): $\{\varepsilon\} = [\boldsymbol{a}_{ij}]\{\sigma\}$.

The stresses and strains in the material coordinate system (x, y, z) are calculated as

$$\begin{Bmatrix} \varepsilon_x \\ \varepsilon_y \\ \varepsilon_z \\ \gamma_{yz} \\ \gamma_{zx} \\ \gamma_{xy} \end{Bmatrix} = -\begin{Bmatrix} -1.43\text{E}-5 \\ -6.693\text{E}-3 \\ 0.011 \\ 4.676\text{E}-3 \\ 9.353\text{E}-3 \\ 3.118\text{E}-3 \end{Bmatrix}, \quad \begin{Bmatrix} \sigma_x \\ \sigma_y \\ \sigma_z \\ \tau_{yz} \\ \tau_{zx} \\ \tau_{xy} \end{Bmatrix} = \begin{Bmatrix} 9.789\text{E}+4 \\ 2.447\text{E}+4 \\ 2.203\text{E}+5 \\ 7.342\text{E}+4 \\ 1.468\text{E}+5 \\ 4.895\text{E}+4 \end{Bmatrix}. \tag{32}$$

The shear stresses on the 30 slip planes can now be calculated, using equations (18)–(20), as

$$\begin{Bmatrix} \tau^1 \\ \tau^2 \\ \tau^3 \\ \tau^4 \\ \tau^5 \\ \tau^6 \\ \tau^7 \\ \tau^8 \\ \tau^9 \\ \tau^{10} \\ \tau^{11} \\ \tau^{12} \end{Bmatrix} = \begin{Bmatrix} -5.995\text{E}+4 \\ 1.199\text{E}+5 \\ 5.995\text{E}+5 \\ 3.996\text{E}+4 \\ -1.199\text{E}+5 \\ -1.599\text{E}+5 \\ -5.995\text{E}+4 \\ -3.996\text{E}+4 \\ -9.991\text{E}+4 \\ 0 \\ 0 \\ 0 \end{Bmatrix}, \quad \begin{Bmatrix} \tau^{13} \\ \tau^{14} \\ \tau^{15} \\ \tau^{16} \\ \tau^{17} \\ \tau^{18} \\ \tau^{19} \\ \tau^{20} \\ \tau^{21} \\ \tau^{22} \\ \tau^{23} \\ \tau^{24} \end{Bmatrix} = \begin{Bmatrix} -1.038\text{E}+5 \\ 0 \\ 1.038\text{E}+5 \\ -1.615\text{E}+5 \\ 1.154\text{E}+5 \\ 4.615\text{E}+4 \\ 8.076\text{E}+4 \\ -9.229\text{E}+4 \\ 1.154\text{E}+4 \\ 0 \\ 0 \end{Bmatrix}, \quad \begin{Bmatrix} \tau^{25} \\ \tau^{26} \\ \tau^{27} \\ \tau^{28} \\ \tau^{29} \\ \tau^{30} \end{Bmatrix} = \begin{Bmatrix} 1.384\text{E}+5 \\ -6.922\text{E}+4 \\ 8.652\text{E}+4 \\ -1.73\text{E}+4 \\ 1.557\text{E}+5 \\ -5.191\text{E}+4 \end{Bmatrix}. \tag{33}$$

The engineering shear strains on the 30 slip planes are

$$\begin{Bmatrix}\gamma^1\\ \gamma^2\\ \gamma^3\\ \gamma^4\\ \gamma^5\\ \gamma^6\\ \gamma^7\\ \gamma^8\\ \gamma^9\\ \gamma^{10}\\ \gamma^{11}\\ \gamma^{12}\end{Bmatrix}=\begin{Bmatrix}-9.725E-3\\ 0.017\\ 7.362E-3\\ 8.452E-3\\ -0.011\\ -0.02\\ -2.742E-4\\ -0.012\\ -0.012\\ 9.451E-3\\ 5.907E-3\\ -3.544E-3\end{Bmatrix},\quad \begin{Bmatrix}\gamma^{13}\\ \gamma^{14}\\ \gamma^{15}\\ \gamma^{16}\\ \gamma^{17}\\ \gamma^{18}\\ \gamma^{19}\\ \gamma^{20}\\ \gamma^{21}\\ \gamma^{22}\\ \gamma^{23}\\ \gamma^{24}\end{Bmatrix}=\begin{Bmatrix}-0.014\\ -1.364E-3\\ 0.015\\ -0.018\\ 0.016\\ 1.575E-3\\ 0.014\\ -7.243E-3\\ -6.768E-3\\ -1.364E-3\\ -7.502E-3\\ 8.867E-3\end{Bmatrix},\quad \begin{Bmatrix}\gamma^{25}\\ \gamma^{26}\\ \gamma^{27}\\ \gamma^{28}\\ \gamma^{29}\\ \gamma^{30}\end{Bmatrix}=\begin{Bmatrix}8.818E-3\\ -4.409E-3\\ 5.511E-3\\ -1.102E-3\\ 9.92E-3\\ -3.307E-3\end{Bmatrix}. \tag{34}$$

The normal stresses and strains on the principal and secondary octahedral planes are computed knowing the stresses and strains in the material coordinate system and the direction cosines of the normal to the octahedral planes. The direction cosines of the normal to the four principal octahedral planes are ($l_1 = 0.5773$, $m_1 = 0.5773$, $n_1 = 0.5773$), ($l_2 = -0.5773$, $m_2 = 0.5773$, $n_2 = -0.5773$), ($l_3 = 0.5773$, $m_3 = -0.5773$, $n_3 = -0.5773$), and ($l_4 = -0.5773$, $m_4 = -0.5773$, $n_4 = 0.5773$). The four normal stresses, σ_i^n, and strains, ε_i^n, to the principal and secondary octahedral planes are calculated using

$$\sigma_i^n = \sigma_x l_i^2 + \sigma_y m_i^2 + \sigma_z n_i^2 + 2\tau_{yz} m_i n_i + 2\tau_{xz} l_i n_i + 2\tau_{xy} m_i l_i \tag{35}$$

$$\varepsilon_i^n = \varepsilon_x l_i^2 + \varepsilon_y m_i^2 + \varepsilon_z n_i^2 + \gamma_{yz} m_i n_i + \gamma_{xz} l_i n_i + \gamma_{xy} m_i l_i \tag{36}$$
$$i = 1,2,3,4 \quad .$$

The computed normal stress and strain values are

$$\begin{Bmatrix}\sigma_1^n\\ \sigma_2^n\\ \sigma_3^n\\ \sigma_4^n\end{Bmatrix}=\begin{Bmatrix}293{,}700\\ 130{,}500\\ 32{,}630\\ 0\end{Bmatrix},\quad \begin{Bmatrix}\varepsilon_1^n\\ \varepsilon_2^n\\ \varepsilon_3^n\\ \varepsilon_4^n\end{Bmatrix}=\begin{Bmatrix}0.007185\\ 0.001989\\ -0.001128\\ -0.002167\end{Bmatrix}. \tag{37}$$

The normal stresses and strains on the cube slip planes are simply the normal stresses and strains in the material coordinate system along (100), (010), and (001) axes.

4.3 Application of Failure Criteria to Uniaxial LCF Data

Strain controlled LCF tests conducted at 1,200 °F in air for PWA 1480/1493 uniaxial smooth specimens, for four different orientations, is shown in table 5. The four specimen orientations are <001> (5 data points), <111> (7 data points), <213> (4 data points), and <011> (3 data points), for a total of 19 data points. Figure 15 shows the plot of strain range versus cycles to failure. A wide scatter is observed in the data with poor correlation for a power law fit. The first step towards applying the failure criteria discussed in section 3 is to compute the shear and normal stresses and strains on all the 30 slip systems, for each data point, for maximum and minimum test strain values. The example problem in section 4.2.4 details the required calculations. The maximum shear stress and strain for each data point, for minimum and maximum test strain values, is selected from the 30 values corresponding to the 30 slip systems. The maximum normal stress and strain values on the planes where the shear stress is maximum is also noted. These values are tabulated in table 6. Both the maximum shear stress and maximum shear strain occur on the same slip system for the four different configurations examined. For the <001> and <011> configurations, the maximum shear stress and strain occur on the secondary slip system (τ^{14}, γ^{14} and τ^{15}, γ^{15}, respectively). For the <111> and <213> configurations, maximum shear stress and strain occur on the cube slip system (τ^{25}, γ^{25} and τ^{29}, γ^{29}, respectively). Using table 6 the composite failure parameters highlighted in equations (1)–(4) can be calculated and plotted as a function of cycles to failure. In addition to the four failure parameters discussed, some other composite parameters are also plotted as a function of cycles to failure (N). Figures 15–25 correspond to the failure parameters.

Table 5. Strain controlled LCF test data at 1,200 °F for four specimen orientations.

Specimen Orientation	Maximum Test Strain	Minimum Test Strain	*R* Ratio	Strain Range	Cycles to Failure
<001>	0.01509	0.00014	0.01	0.01495	1,326
<001>	0.0174	0.0027	0.16	0.0147	1,593
<001>	0.0112	0.0002	0.02	0.011	4,414
<001>	0.01202	0.00008	0.01	0.0119	5,673
<001>	0.00891	0.00018	0.02	0.00873	29,516
<111>	0.01219	−0.006	−0.49	0.01819	26
<111>	0.0096	0.0015	0.16	0.0081	843
<111>	0.00809	0.00008	0.01	0.00801	1,016
<111>	0.006	0.0	0.0	0.006	3,410
<111>	0.00291	−0.00284	−0.98	0.00575	7,101
<111>	0.00591	0.00015	0.03	0.00576	7,356
<111>	0.01205	0.00625	0.52	0.0058	7,904
<213>	0.01212	0.0	0.0	0.01212	79
<213>	0.00795	0.00013	0.02	0.00782	4,175
<213>	0.00601	0.00005	0.01	0.00596	34,676
<213>	0.006	0.0	0.0	0.006	114,789
<011>	0.0092	0.0004	0.04	0.0088	2,672
<011>	0.00896	0.00013	0.01	0.00883	7,532
<011>	0.00695	0.00019	0.03	0.00676	30,220

Table 6. Maximum values of shear stress and shear strain on the slip systems and normal stress and strain values on the same planes.

γ_{max} = Max shear strain of 30 slip systems for max specimen test strain value
γ_{min} = Max shear strain of 30 slip systems for min specimen test strain value
τ_{max} = Max shear stress of 30 slip systems for max specimen test strain value
τ_{min} = Max shear stress of 30 slip systems for min specimen test strain value

Specimen Orientation	γ_{max}	γ_{min}	$\Delta\gamma/2$	ε_{max}	ε_{min}	$\Delta\varepsilon/2$	τ_{max} (psi)	τ_{min} (psi)	$\Delta\tau$ (psi)	σ_{max} (psi)	σ_{min} (psi)	$\Delta\sigma$ (psi)	Cycles to Failure
<001>	0.02	0.000185	0.0099075	0.00097	9.25E–06	0.0004804	1.10E+05	1016	1.08E+05	7.75E+04	719	7.68E+04	1,326
	0.023	0.0036	0.0097	0.0015	1.78E–04	0.000661	1.26E+05	1.96E+04	1.06E+05	8.93E+04	1.39E+04	7.54E+04	1,593
$\tau_{max} = \tau^{14}$	0.015	2.64E–04	0.007368	7.34E–04	1.32E–05	0.0003604	8.13E+04	1452	7.98E+04	5.75E+04	1027	5.65E+04	4,414
$\gamma_{max} = \gamma^{14}$	0.016	0	0.008	7.94E–04	0	0.000397	8.73E+04	0	8.73E+04	6.17E+04	0	6.17E+04	5,673
	0.012	0	0.006	5.89E–04	0	0.0002945	6.47E+04	0	6.47E+04	4.57E+04	0	4.57E+04	29,516
<111>	0.014	–7.06E–03	0.01053	2.05E–03	–1.01E–03	0.00153	2.25E+05	–1.10E+05	3.35E+05	1.59E+05	–7.80E+04	2.37E+05	26
	0.011	0.00176	0.00462	0.0016	0.00025	0.000675	1.77E+05	2.77E+04	1.49E+05	1.25E+05	1.96E+04	1.05E+05	843
$\tau_{max} = \tau^{25}$	0.0095	9.40E–05	0.004703	0.00136	1.34E–05	0.0006733	1.49E+05	1478	1.48E+05	1.06E+05	1045	1.05E+05	1,016
$\gamma_{max} = \gamma^{25}$	0.0076	0	0.0038	0.001	0	0.0005	1.10E+05	0	1.10E+05	7.84E+04	0	7.84E+04	,3410
	0.0034	–0.0033	0.00335	0.00049	–0.00048	0.000485	5.40E+04	–5.30E+04	1.07E+05	3.80E+04	–3.70E+04	7.50E+04	7,101
	0.0069	1.76E–04	0.003362	9.90E–04	2.50E–05	0.0004825	1.09E+05	2771	1.06E+05	7.70E+04	1959	7.50E+04	7,356
	0.014	0.007	0.0035	0.002	0.001	0.0005	2.25E+05	1.10E+05	1.15E+05	1.60E+05	7.80E+04	8.20E+04	7,904
<213>	0.018	0	0.009	0.002	0	0.001	1.60E+05	0	1.60E+05	1.30E+05	0	1.30E+05	79
	0.012	1.90E–04	0.005905	0.0013	2.10E–05	0.0006395	1.06E+05	1732	1.04E+05	8.60E+04	1400	8.46E+04	4,175
$\tau_{max} = \tau^{29}$	0.0088	0	0.0044	0.00098	0	0.00049	8.00E+04	0	8.00E+04	6.50E+04	0	6.50E+04	34,676
$\gamma_{max} = \gamma^{29}$	0.0088	0	0.0044	0.00098	0	0.00049	8.00E+04	0	8.00E+04	6.50E+04	0	6.50E+04	114,789
<011>	0.015	6.50E–04	0.007175	0.0039	1.68E–04	0.001866	1.23E+05	5333	1.18E+05	1.73E+05	7538	1.65E+05	2,672
$\tau_{max} = \tau^{15}$	0.015	0	0.0075	0.0039	0	0.00195	1.23E+05	0	1.23E+05	1.70E+05	0	1.70E+05	7,532
$\gamma_{max} = \gamma^{15}$	0.011	3.10E–04	0.005345	0.0029	8.00E–05	0.00141	9.30E+04	2532	9.05E+04	1.31E+05	3581	1.27E+05	30,220

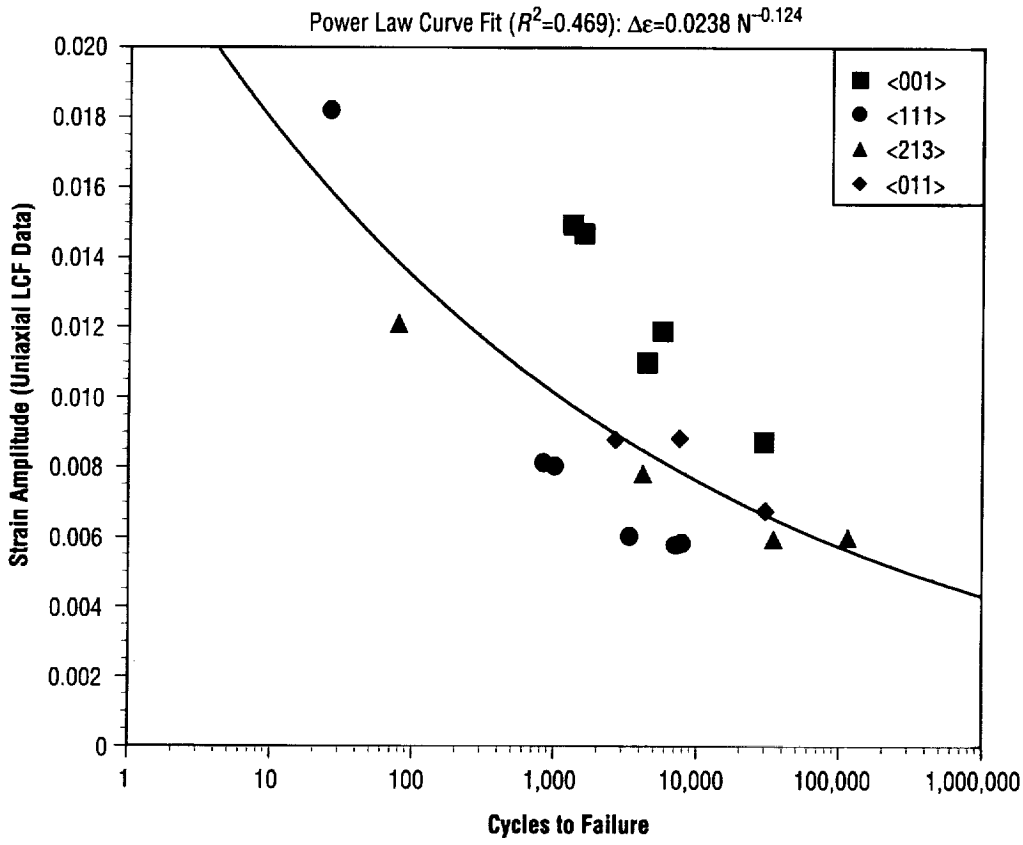

Figure 15. Strain range versus cycles to failure for LCF test data (PWA 1493 at 1,200 °F).

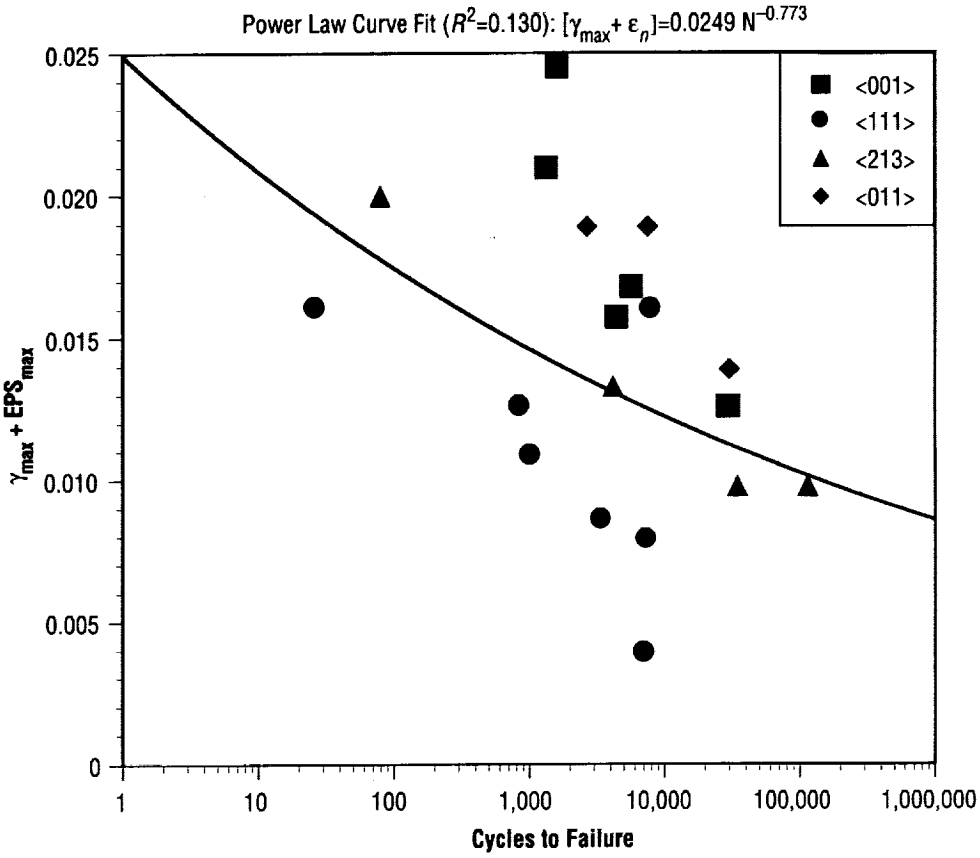

Figure 16. $[\gamma_{max}+\varepsilon_n]$ (eqn. (35)) versus N.

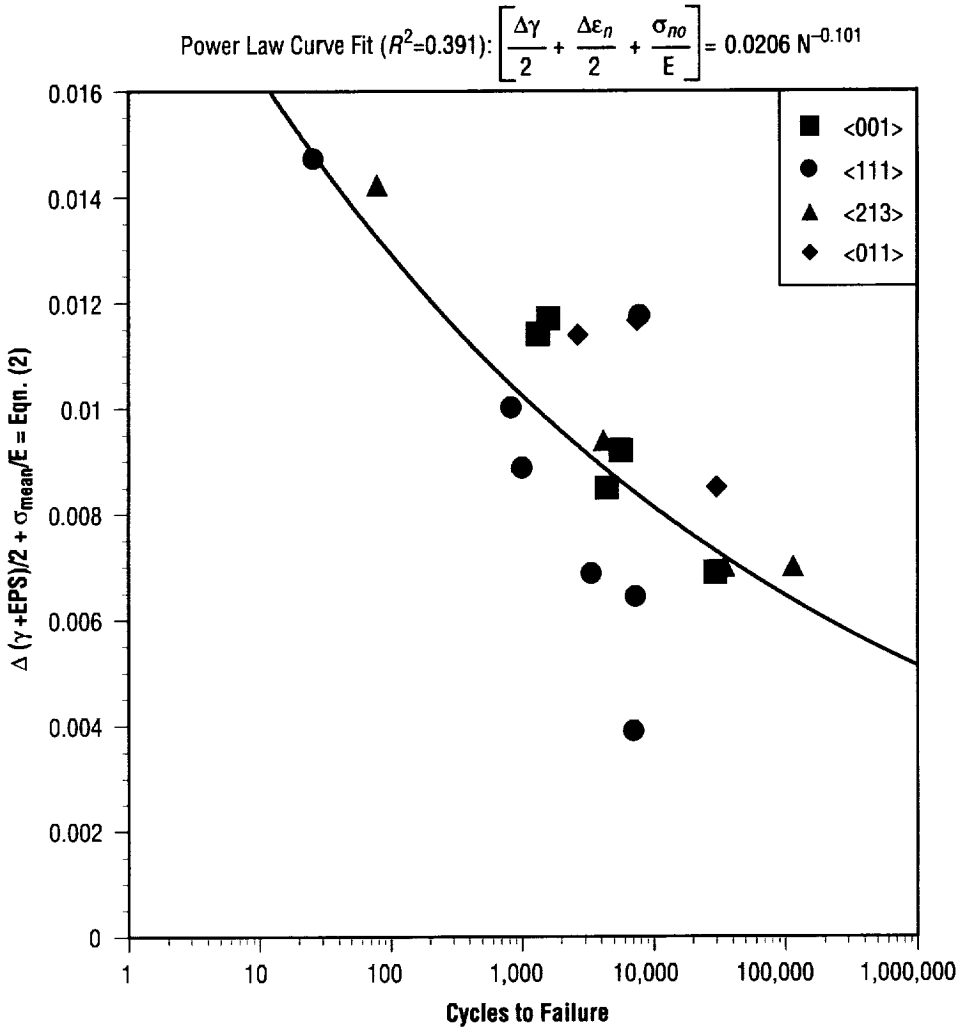

Figure 17. $\left[\frac{\Delta\gamma}{2}+\frac{\Delta\varepsilon_n}{2}+\frac{\sigma_{no}}{E}\right]$ (eqn. (36)) versus N.

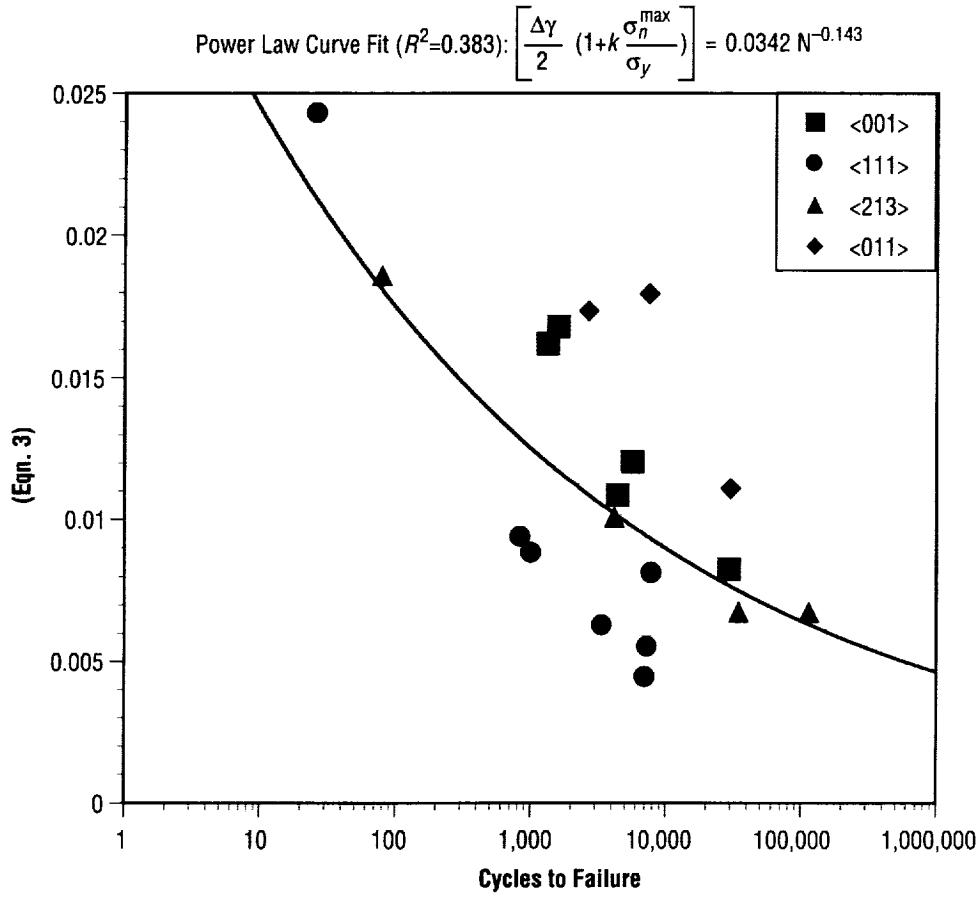

Figure 18. $\left[\frac{\Delta\gamma}{2}(1+k\frac{\sigma_n^{max}}{\sigma_y})\right]$ (eqn. (37)) versus N.

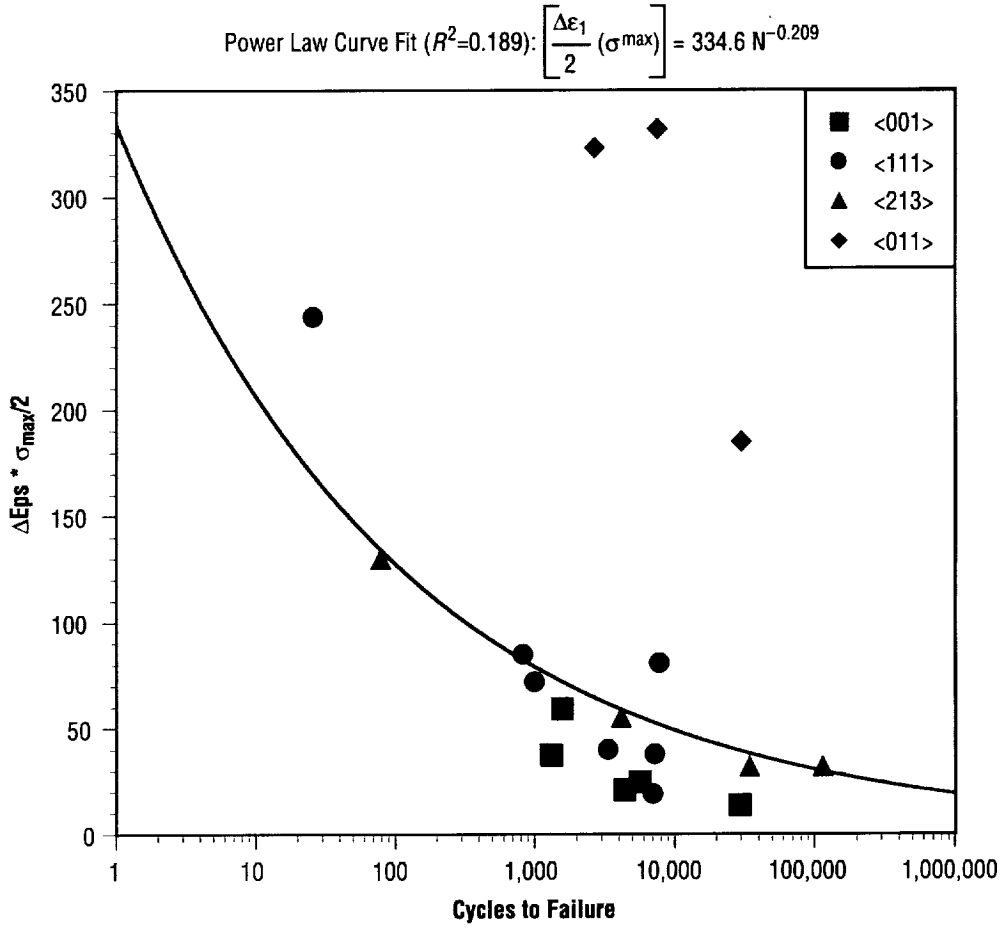

Figure 19. $\left[\frac{\Delta\varepsilon_1}{2}\left(\sigma^{\max}\right)\right]$ (eqn. (38)) versus N.

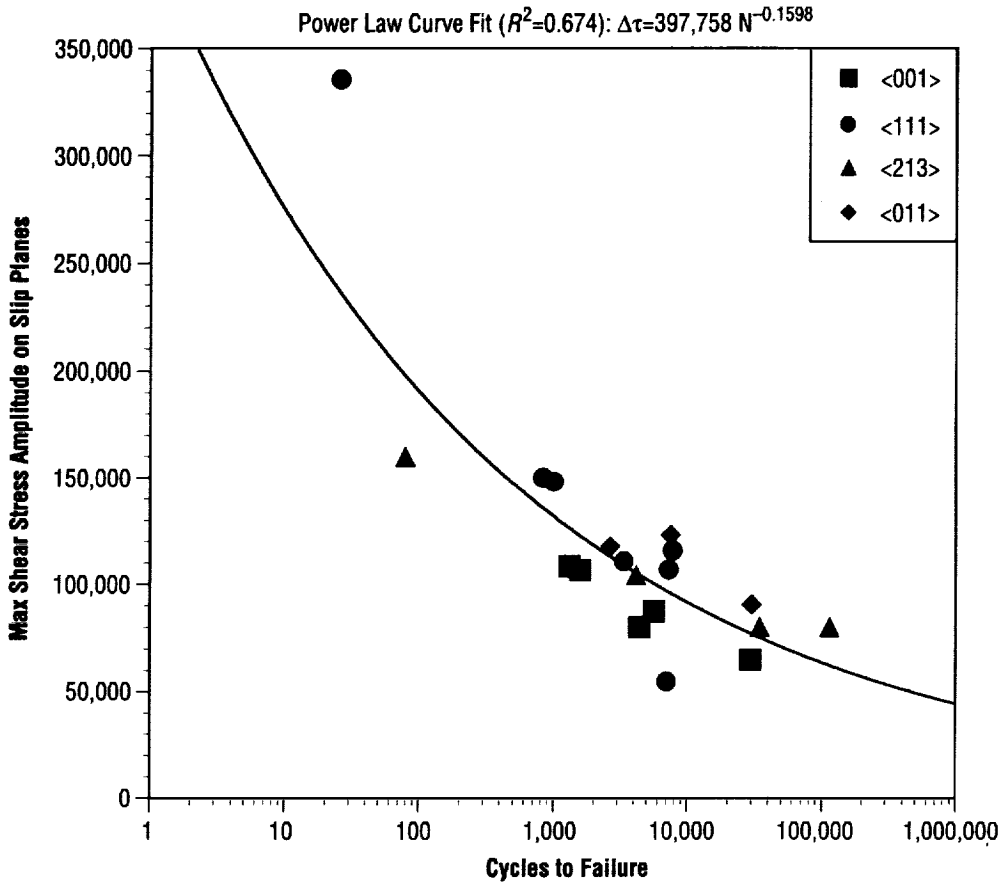

Figure 20. Shear stress amplitude [$\Delta\tau_{max}$] versus N.

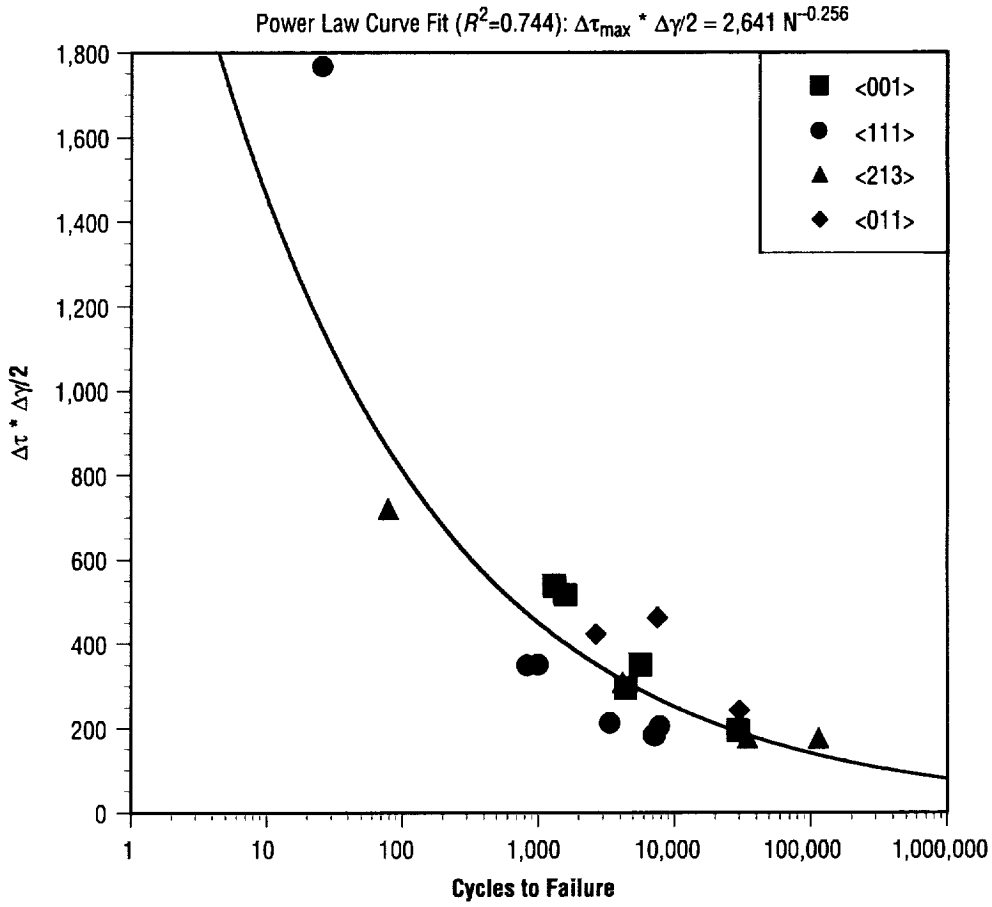

Figure 21. $\left[\Delta\tau_{\max}\frac{\Delta\gamma_{\max}}{2}\right]$ versus N.

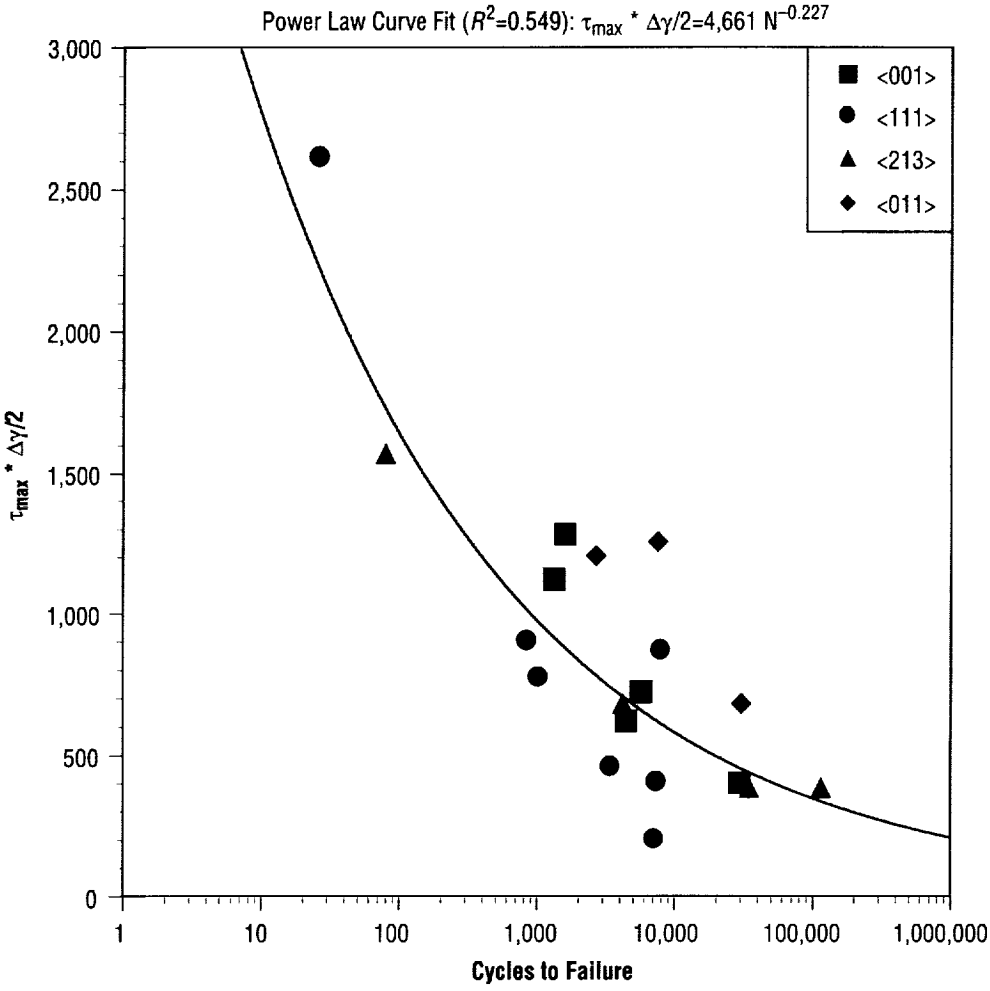

Figure 22. $\left[\tau_{\max}\frac{\Delta\gamma_{\max}}{2}\right]$ versus N.

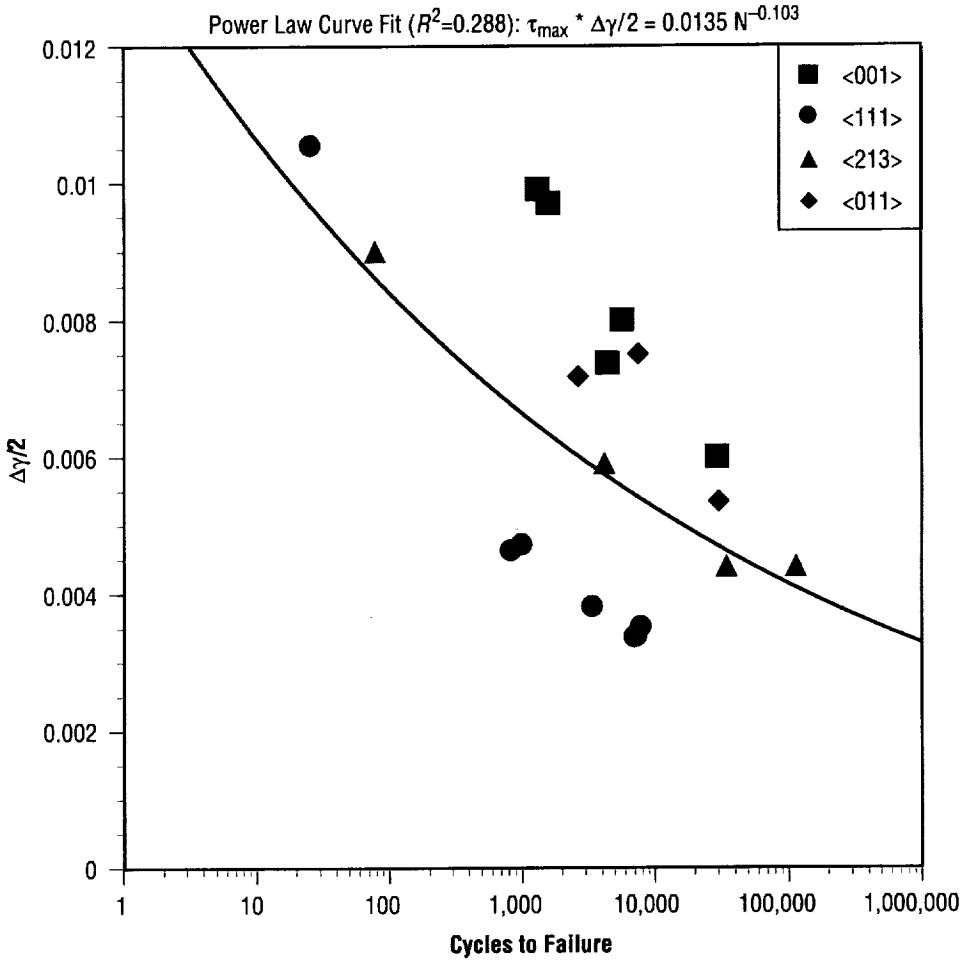

Figure 23. Shear strain amplitude $\left[\frac{\Delta\gamma_{max}}{2}\right]$ versus N.

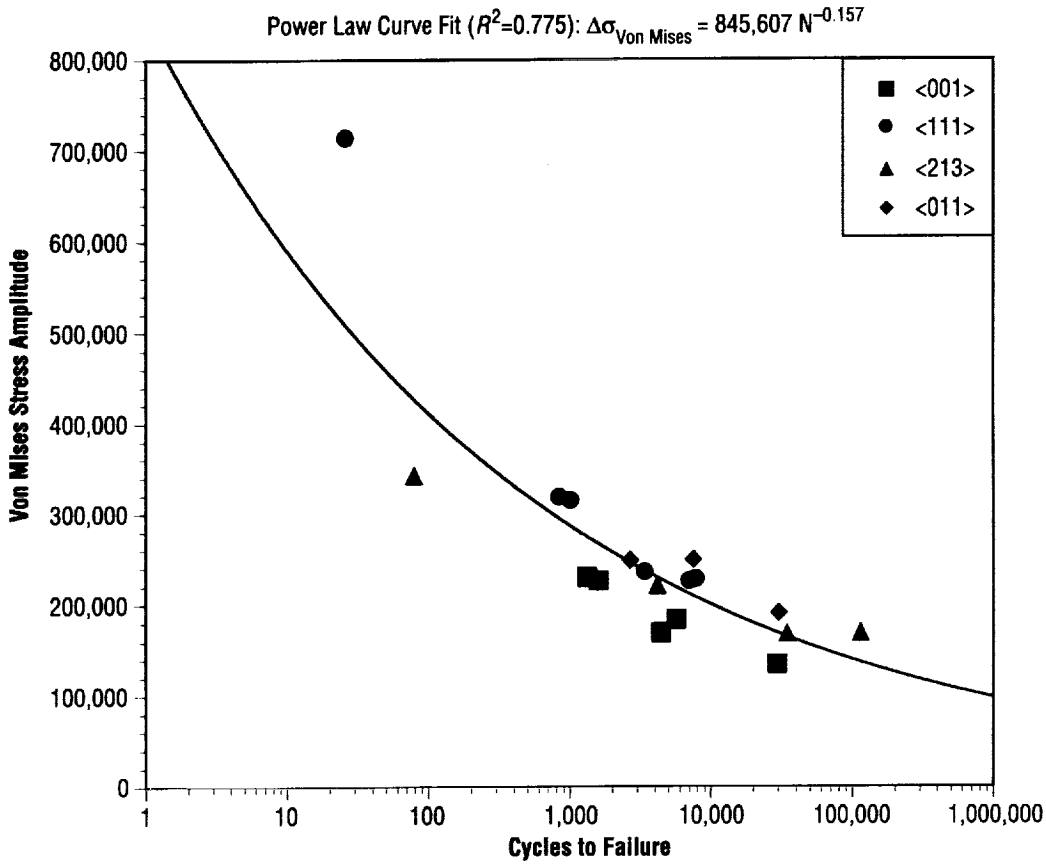

Figure 24. $\Delta\sigma_{Von\ Mises}$ versus N.

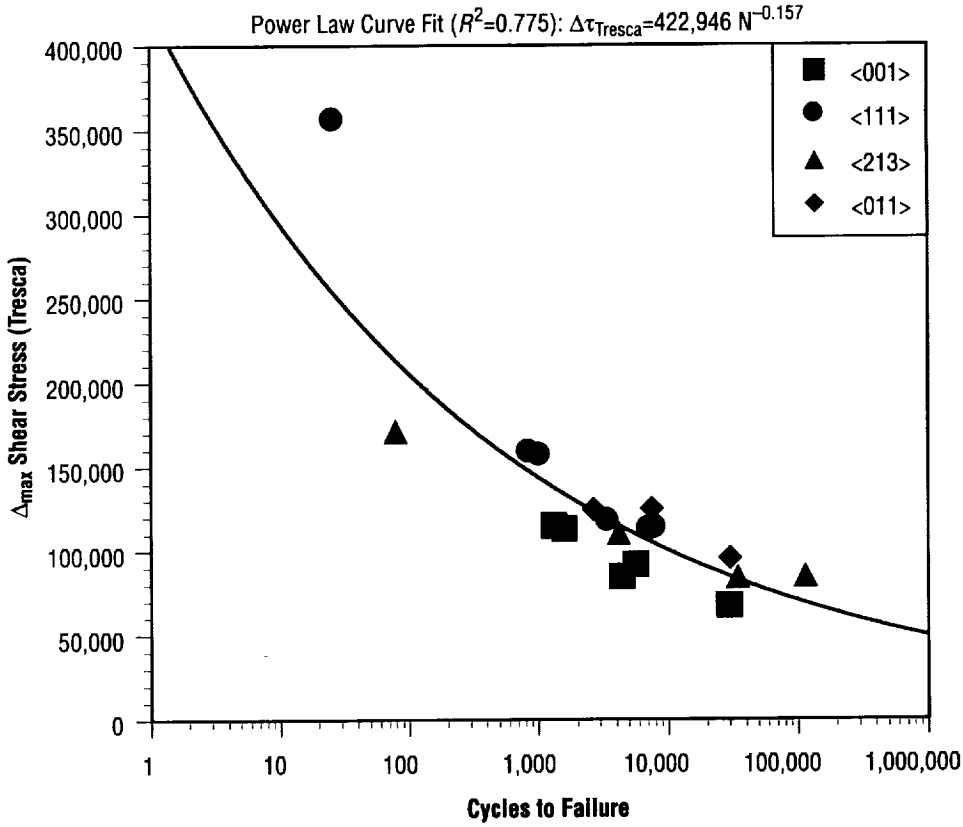

Figure 25. $\Delta\tau_{Tresca}$ versus N.

The power law curve fits for the parameters and their correlation coefficients are listed in table 7. From figures 16–19 we can see that the four parameters based on polycrystalline fatigue failure parameters do not correlate well with the test data. The application of these parameters for single crystal material is somewhat different since they are evaluated on the slip systems that are thought to be the critical planes. For polycrystalline materials, the critical plane has to be searched for to find the plane that yields the maximum value of the failure parameter. The parameters that collapse the failure data well and give the best correlation with a power law fit are the maximum shear stress amplitude [$\Delta\tau_{max}$] shown in figure 20, and the composite parameter $\left[\Delta\tau_{max}\frac{\Delta\gamma_{max}}{2}\right]$ shown in figure 21, the Von Mises equivalent stress amplitude shown in figure 24, and the maximum principal shear stress amplitude (Tresca theory) shown in figure 25. The parameter $\Delta\tau_{max}$ is appealing to use for its simplicity, and its power law curve fit is shown in equation (38):

$$\Delta\tau_{max} = 397{,}758\ N^{-0.1598}\ . \tag{38}$$

It must be remembered that these curve fits are only valid for 1,200 °F. The correlation for [$\Delta\tau_{max}$] would be better if some of the high stress data points are corrected for inelastic effects. Since the deformation mechanisms in single crystals are controlled by the propagation of dislocations driven by shear, the [$\Delta\tau_{max}$] might indeed be a good fatigue failure parameter to use. This parameter must be verified for a wider range of R-values and specimen orientations, and also at different temperatures and environmental conditions. Equation (38) gives a useful relation that can be used to calculate fatigue life for PWA 1493 at 1,200 °F. This relation will be used to calculate fatigue life at a critical blade tip location for the SSME turbine blade.

Table 7. Power law curve fits for the failure parameters

Correlation Coefficient, R^2	Power Law Curve Fit
0.468	Strain Range, $\Delta\varepsilon = 0.0238\ N^{-0.124}$
0.130	$[\gamma_{max} + \varepsilon_n] = 0.0249\ N^{-0.773}$
0.391	$\left[\frac{\Delta\gamma}{2} + \frac{\Delta\varepsilon_n}{2} + \frac{\sigma_{no}}{E}\right] = 0.0206\ N^{-0.101}$
0.383	$\left[\frac{\Delta\gamma}{2}\left(1 + k\frac{\sigma_n^{max}}{\sigma_y}\right)\right] = 0.0342\ N^{-0.143}$
0.189	$\left[\frac{\Delta\varepsilon_1}{2}\left(\sigma^{max}\right)\right] = 334.6\ N^{-0.209}$
0.674	$\Delta\tau_{max} = 397{,}758\ N^{-0.1598}$ (Max shear stress amplitude of 30 slip systems)
0.744	$\Delta\tau_{max} * \Delta\gamma/2 = 2{,}641\ N^{-0.256}$
0.549	$\tau_{max} * \Delta\gamma/2 = 4{,}661\ N^{-0.227}$
0.775	$\Delta\sigma_{Von\ Mises} = 845{,}607\ N^{-0.157}$ (Equivalent stress (Von Mises) amplitude)
0.775	$\Delta\tau_{Tresca} = 422{,}946\ N^{-0.157}$ (Max principal shear stress amplitude)

5. APPLICATION OF FATIGUE FAILURE CRITERIA TO FINITE ELEMENT STRESS ANALYSIS RESULTS OF SINGLE-CRYSTAL NICKEL TURBINE BLADES

5.1 Introduction

Turbine blades used in the high-pressure fuel turbopump/alternate turbopump (HPFTP/AT) are fabricated from single-crystal Ni PWA 1493 material. In September 1997, an HPFTP/AT for the SSME suffered a turbine blade failure during development testing. These turbopumps are critical to engine operation and failure of the unit is a significant risk to the Shuttle mission. Similar blade failures occurring in units of the initial design resulted in catastrophic engine failure. The subsequent investigation into the blade failure provided insight into areas where the robustness of the design could be improved to reduce the potential for failure.[3]

Cause of the blade failure in the HPFTP/AT was determined to be the initiation and propagation of fatigue cracks from an area of high concentrated stress at the blade tip leading edge. Figure 26 shows the blade tip crack location and orientation. Inspection of blades from other units in the test program revealed the presence of similar cracks in the turbine blades. During the course of the investigation, an interesting development was brought to light. When the size of the fatigue cracks for the population of blades inspected was compared with the secondary crystallographic orientation, β, a definite relationship was apparent, as shown in figure 26.[3] Secondary orientation does appear to have some influence over whether a crack will initiate and arrest or continue to grow until failure of the blade airfoil occurs. Figure 26 reveals that for $\beta = 45° \pm 15°$ tip cracks arrested after some growth or did not initiate at all. This suggests that perhaps there are preferential β orientations for which crack growth is minimized at the blade tip. The data obtained while intriguing are only applicable to that particular blade design and at the location where the cracks initiated.

In an attempt to understand the effect of secondary orientation on blade stress response, this section describes an FE model capable of accounting for secondary orientation variation. Fatigue failure criteria developed in section 4 will be applied to blade tip stress results at the critical location, in an attempt to explain figure 26 from analytical modeling. Additionally, stress analysis results from the blade attachment region will also be examined in view of their susceptibility to initiate cracks from fretting fatigue.

5.2 Description of the Finite Element Model

The HPFTP/AT first stage blade ANSYS finite element model (FEM) was cut from a large three-dimensional cyclic symmetry model that includes the first and second stage blades and retainers, interstage spacer, disk and shaft, and the disk covers. The blade dampers are represented with forces applied to the blade platforms at the damper contact locations. The models are geometrically nonlinear due to the contact surfaces between the separate components. The large model was developed by ADAPCO for Pratt and Whitney as part of the critical design review (CDR) for the HPFTP/AT and is shown in figure 27.[18] Due to the large size of the global model, cutting the first stage blade from it was necessary to reduce the computer run time and file size required for the multiple runs needed to study the effect of material orientation.

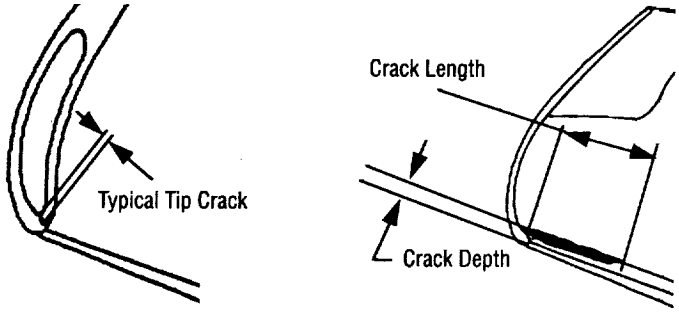

Blade Leading Edge Crack Location and Orientation

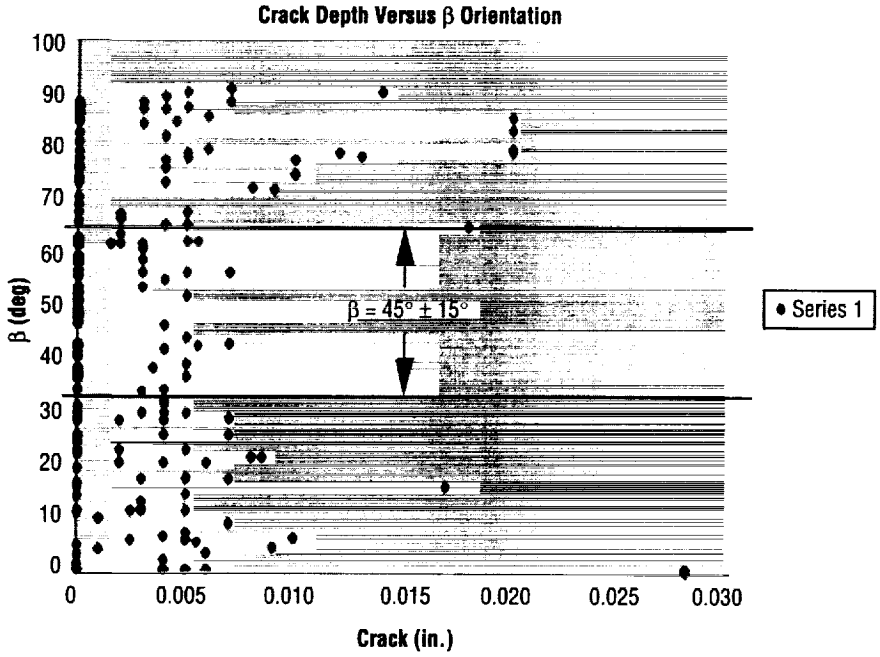

Figure 26. Secondary crystallographic orientation, β, versus crack depth for the SSME HPFTP/AT first stage turbine blade.[3]

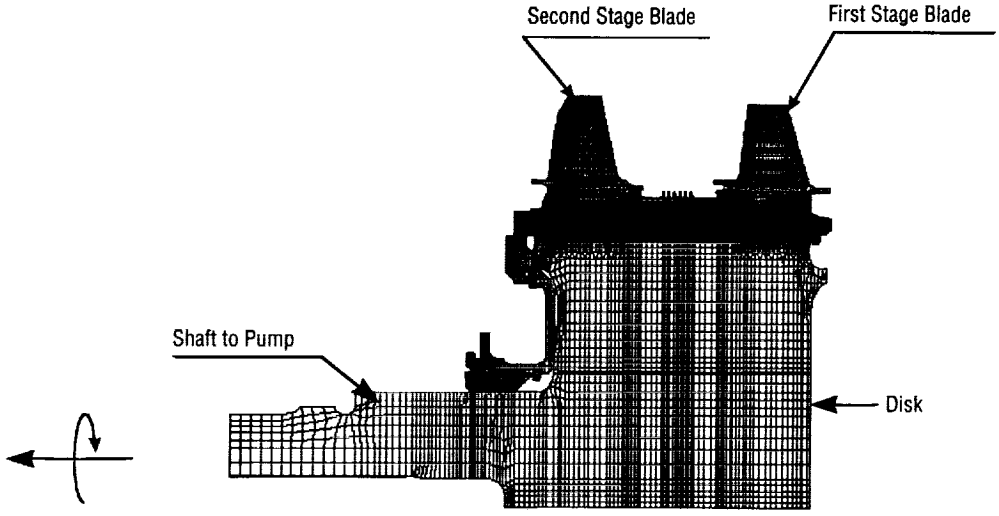

Figure 27. Three-dimensional ANSYS model of HPFTP/AT rotating turbine components.

The element type used for the blade material is the ANSYS SOLID45, an eight-node, three-dimensional solid isoparametric element with internal extra shape functions. Anisotropic material properties are allowed with this element type; the ANSYS program aligns the material coordinate system with the element coordinate system. To generate the 297 material coordinate systems used for this study, local coordinate systems were generated and the element coordinate systems aligned with them.[19] The material coordinate system is referenced to the blade casting coordinate system shown in figure 28. It should be noted that the first and the second stage blades do not share the same casting coordinate systems. The relative orientation of the primary axis of the material coordinate system to the casting coordinate system is shown in figure 29. Two angles, Δ and γ, locate the primary material axis relative to the casting axis; the third angle, β, is the clocking of the secondary material axis about the primary material axis. Figure 30 and table 8 show the distribution of the 297 different material coordinate systems within the allowed 15° maximum deviation from the casting axis. The secondary repeats after 90°, so only 0° to 80° needed to be modeled.

First Stage Blade Casting Coordinate System (CS 30)
z axis along stacking axis pointing radially inward
x axis pointing away from the pressure side
y axis pointing towards the second stage blade

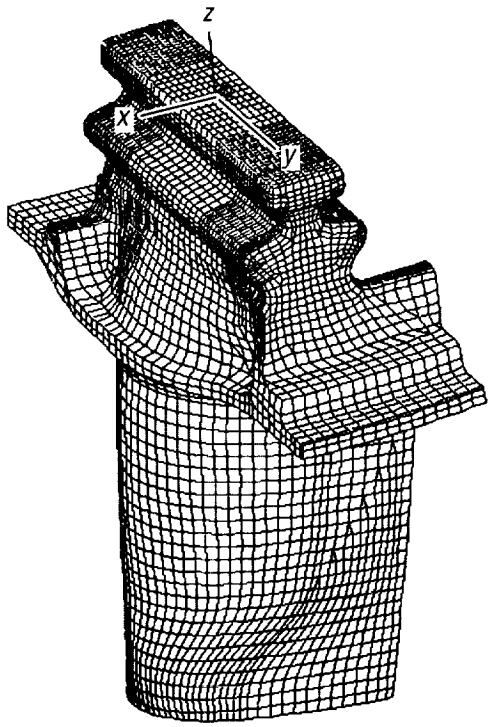

Figure 28. First stage blade casting coordinate system.

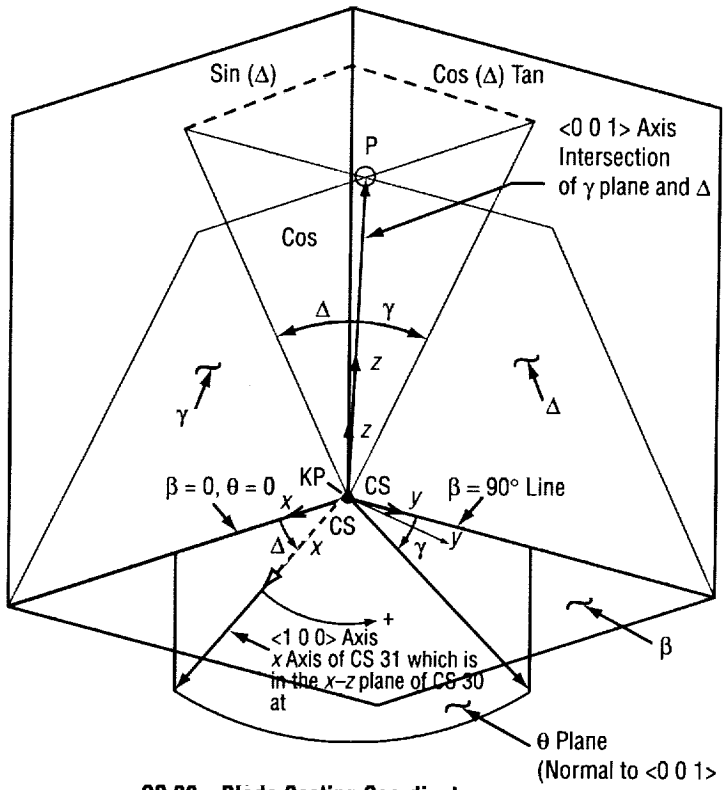

Figure 29. First stage blade material coordinate system relative to the casting coordinate system.

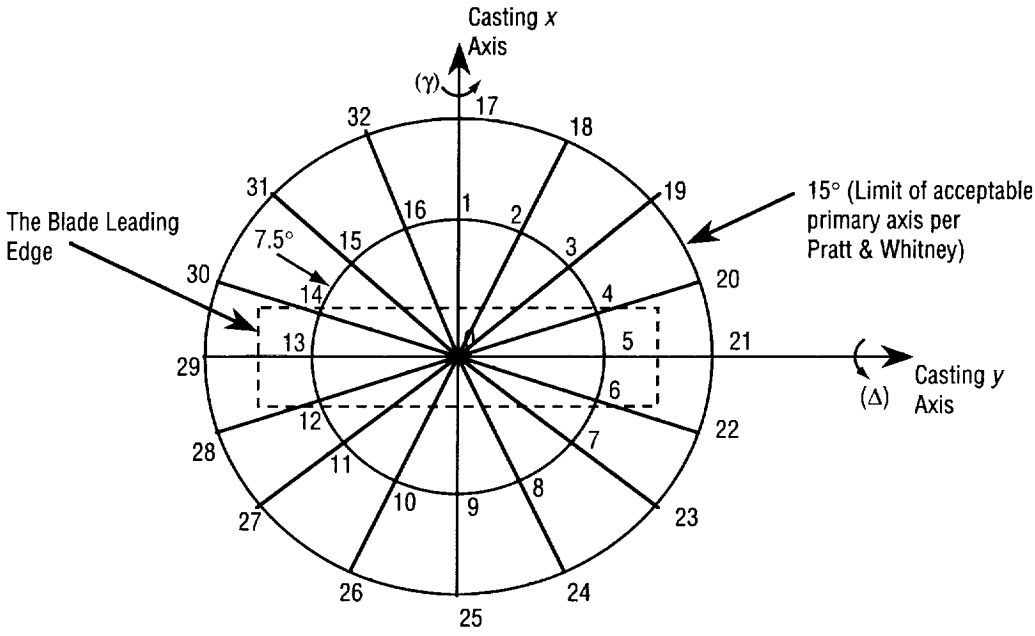

Top View of the Blade

- 33 orientations (cases) of (γ and Δ) with 9 (θ)orientations about each of these.
  - 16 cases with (γ and Δ) combined to 7.5°, 16 with (γ and Δ) combined to 15°, 1 case with (γ and Δ) combined to 0°.
  - (θ) varied from 0° to 80° in 10° increments about the local material axis (due to symmetry, 90° is the same as 0°).
- Total of 297 orientations.

Figure 30. Thirty-three primary axis cases with nine secondary cases each, a total of 297 material orientations.

Table 8. Thirty-three primary axis cases with nine secondary cases each, a total of 297 material orientations.

Case	Δ	γ	β
0	0.00	0.00	0,10,20,30,40,50,60,70,80
1	7.50	0.00	0,10,20,30,40,50,60,70,80
2	6.93	2.87	0,10,20,30,40,50,60,70,80
3	5.30	5.30	0,10,20,30,40,50,60,70,80
4	2.87	6.93	0,10,20,30,40,50,60,70,80
5	0.00	7.50	0,10,20,30,40,50,60,70,80
6	−2.87	6.93	0,10,20,30,40,50,60,70,80
7	−5.30	5.30	0,10,20,30,40,50,60,70,80
8	−6.93	2.87	0,10,20,30,40,50,60,70,80
9	−7.50	0.00	0,10,20,30,40,50,60,70,80
10	−6.93	−2.87	0,10,20,30,40,50,60,70,80
11	−5.30	−5.30	0,10,20,30,40,50,60,70,80
12	−2.87	−6.93	0,10,20,30,40,50,60,70,80
13	0.00	−7.50	0,10,20,30,40,50,60,70,80
14	2.87	−6.93	0,10,20,30,40,50,60,70,80
15	5.30	−5.30	0,10,20,30,40,50,60,70,80
16	6.93	−2.87	0,10,20,30,40,50,60,70,80
17	15.00	0.00	0,10,20,30,40,50,60,70,80
18	13.86	5.74	0,10,20,30,40,50,60,70,80
19	10.61	10.61	0,10,20,30,40,50,60,70,80
20	5.74	13.86	0,10,20,30,40,50,60,70,80
21	0.00	15.00	0,10,20,30,40,50,60,70,80
22	−5.74	13.86	0,10,20,30,40,50,60,70,80
23	−10.61	10.61	0,10,20,30,40,50,60,70,80
24	−13.86	5.74	0,10,20,30,40,50,60,70,80
25	−15.00	0.00	0,10,20,30,40,50,60,70,80
26	−13.86	−5.74	0,10,20,30,40,50,60,70,80
27	−10.61	−10.61	0,10,20,30,40,50,60,70,80
28	−5.74	−13.86	0,10,20,30,40,50,60,70,80
29	0.00	−15.00	0,10,20,30,40,50,60,70,80
30	5.74	−13.86	0,10,20,30,40,50,60,70,80
31	10.61	−10.61	0,10,20,30,40,50,60,70,80
32	13.86	−5.74	0,10,20,30,40,50,60,70,80

The boundary conditions represent full power mainstage operation of the SSME, referred to as 109-percent rated power level service life (RPL SL). The shaft speed is 37,355 rpm, the airfoil temperature is ≈1,200 °F, forces representing the blade damper radial sling load are applied to the blade platform, and pressures are applied to the blade surfaces and internal core.

The 297 finite element results files presented a difficult challenge to post process. Two FORTRAN codes, developed at Marshall Space Flight Center, were employed for this effort. The first strips the element results from the coded binary output files and places them into ASCII text files. The second program processes the ASCII files to calculate averaged nodal results, the resolved shear stresses and strains, and the normal stresses and strains in the single-crystal material coordinate system. It then calculates the parameters chosen for study and sorts them based on user set criteria.

The connection between the blade and disk are modeled with ANSYS COMBIN40 elements. These elements have 1 degree of freedom (DOF) at each node. The nodal motion in that DOF sets the separation or contact of these elements only. This element does not have the capability for friction tangent to the contact surface. For this model, the nodal coordinate systems on the contacting surface of the blade firtree attachment were rotated so that one axis is normal to the surface. This is the DOF used in the COMBIN40 element. The nodal coordinate systems on the disk contact surfaces were similarly oriented. An interesting feature of the ADAPCO model is that the blade is next to a cyclic symmetry section of the disk (a 1-of-50 piece) so that only the pressure side of the blade attachment contact surface nodes are nearly coincident to the disk. The suction side of the blade is clocked 7.2° about the shaft from the mating surface on the disk. The blade and disk nodal coordinate systems for the suction side attachment are 7.2° out of parallel to each other to account for this. Since the COMBIN40 element only acts on the 1 DOF normal to the contact surfaces, the 7.2° offset in physical location and orientation is properly accounted for. To run the blade model separate from the global model, the nodal displacements of the disk nodes attached to the COMBIN40 elements were taken from a run of the global model and used as enforced displacements for what would become free ends of the contact elements.

For the portion of this study that requires friction, the COMBIN40 element was replaced with CONTAC52 type elements. The CONTAC52 element has 3 DOF at each node, allows a coefficient of friction to develop forces tangential to the normal force, and uses the relative position and motion of the end nodes to define displacement and reaction force magnitude and direction. Since 1,030 nodes were located 7.2° away from being coincident with the suction side of the blade, these nodes were modified to bring them into alignment. If they were not moved, the line of action of the contact element would not simulate the mating surfaces between the blade and disk. The imposed displacements on the nodes representing the disk were not corrected for the 7.2° change in position, so the line of action of the mating surface does contain a built-in offset. For a qualitative comparison of variation of friction coefficient at the contact region on stress distribution and material orientation, this error was ignored. However, the offset will need to be corrected if a contact analysis using friction is required for more than a comparative analysis.

Postprocessing of the friction data was performed by constructing a local coordinate system with one axis in the tangential direction of contact slip on the blade attachment (fig. 31). An ANSYS batch-postprocessing routine was written to output tabulated results for selected nodes in the attachment.

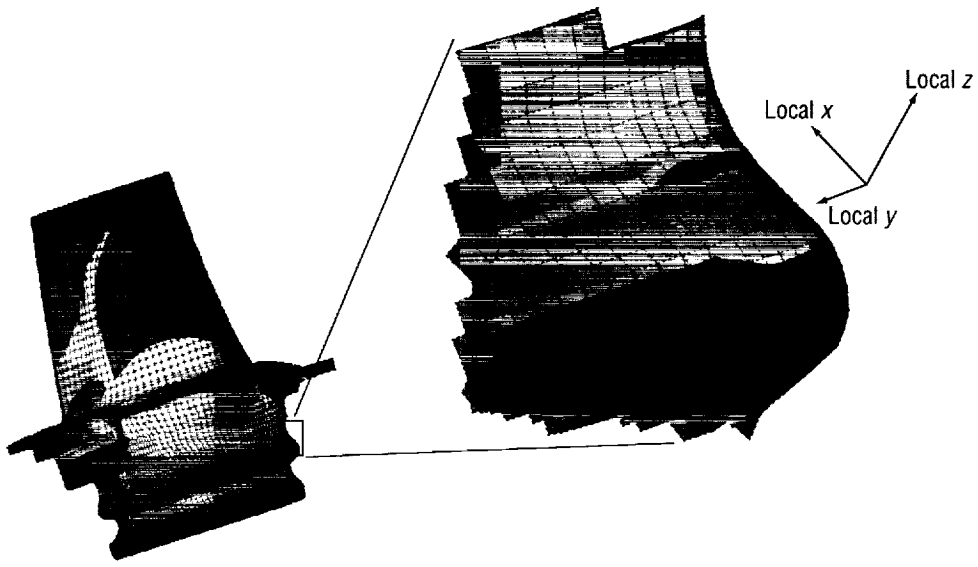

Figure 31. HPFTP/AT first blade Von Mises stress plot with local zoom in of the suction side upper contact region at the blade leading edge and the local coordinate system used for the contact result.

5.3 Finite Element Model Stress Analysis Results

Figure 32 shows representative Von Mises stress distribution plot for the turbine blade in the attachment region. The crack location and orientation at the critical blade tip location is shown in figure 26. Effect of secondary orientation variation on stress response at the blade tip critical point is discussed first, followed by a discussion of stresses in the blade attachment region (contact points).

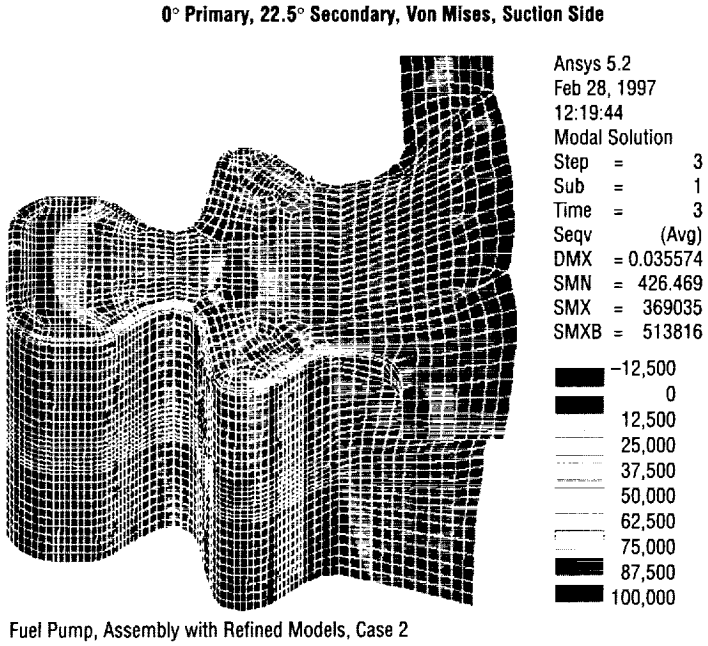

Figure 32. Representative Von Mises stress distribution results in the blade attachment region.

5.3.1 Effect of Secondary Crystal Orientation on Blade Tip Stress Response

The blade tip cracking experience, which is shown in figure 26 for units F3–4B and F6–5D, was segregated into the closest case number for each blade's primary orientation, per figure 30. The crack length was contour plotted as a function of case number and secondary angle, β, and is shown in figure 33. The actual blade data does not have primary orientations that come close to the specification limit of 15 degrees off of the blade stacking axis, so no engine test blade data are available for case numbers over 16. This is why the upper part of the plot in figure 33 is void of data.

Variation of secondary crystal orientation on stress response at the blade tip critical point prone to cracking (tip point on inside radius) was examined by analyzing the results from the 297 FE model runs. The FE node at the critical point was isolated and critical failure parameter value ($\Delta\tau_{max}$) computed on the 30 slip systems, as explained in section 4. A contour plot of $\Delta\tau_{max}$ was generated as a function of primary and secondary orientation, shown in figure 34. The contour plot clearly shows a minimum value for $\Delta\tau_{max}$ for secondary orientation of $\beta = 50°$ and primary orientation designated by cases 5 and 20. From table 8 we see that case 5 corresponds to a primary orientation of $\Delta = 0°$ and $\gamma = 7.5°$. Case 20 corresponds to a primary orientation of $\Delta = 5.74°$ and $\gamma = 13.86°$. Using the fatigue life equation based on the $\Delta\tau_{max}$ curve fit of LCF test data, equation (38), we can obtain a contour plot of dimensionless life at the critical point as a function of primary and secondary orientation, as shown in figure 35. The maximum life is again obtained for $\beta = 50°$, and $\Delta = 0°$ and $\gamma = 7.5°$, and $\Delta = 5.74°$ and $\gamma = 13.86°$. The optimum value of secondary orientation $\beta = 50°$ corresponds very closely to the optimum value of β indicated in figure 33. This demonstrates that control of secondary and primary crystallographic orientation has the potential to significantly increase a component's resistance to fatigue crack growth without adding additional weight or cost.

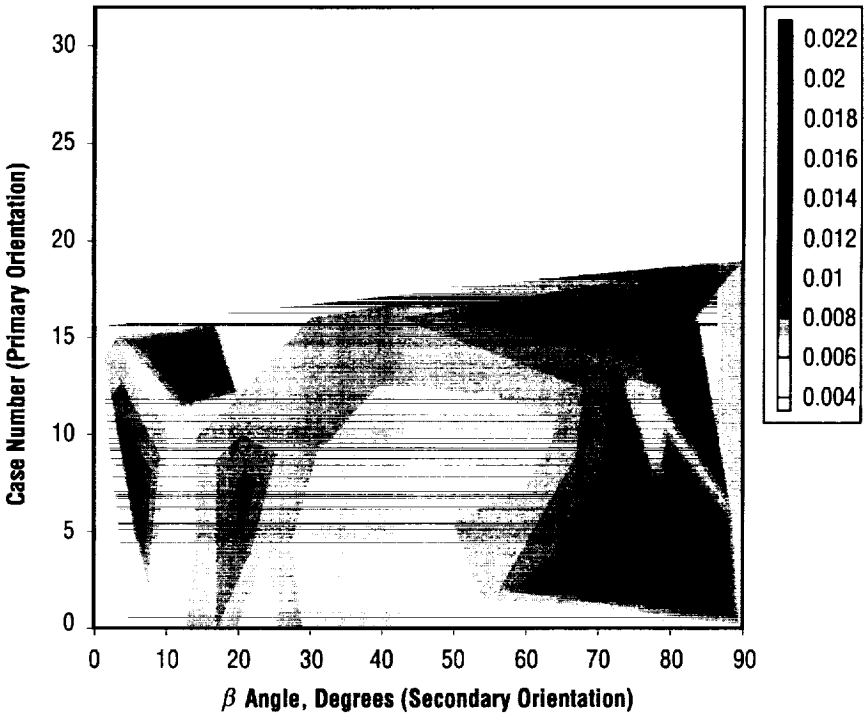

Figure 33. F3–4B and FG–5D first blades xxx FPI data. Contour plot of crack length across blade wall in inches (0.02 is through wall for this plot).

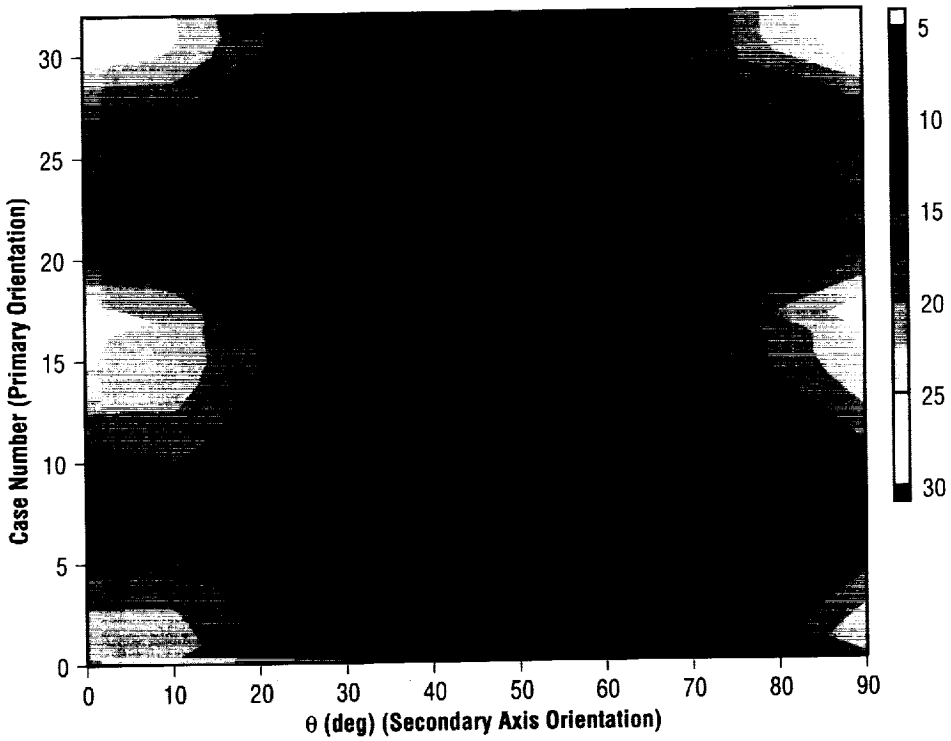

Figure 34. Maximum shear stress amplitude ($\Delta\tau_{max}$, ksi) contour at the blade tip critical point.

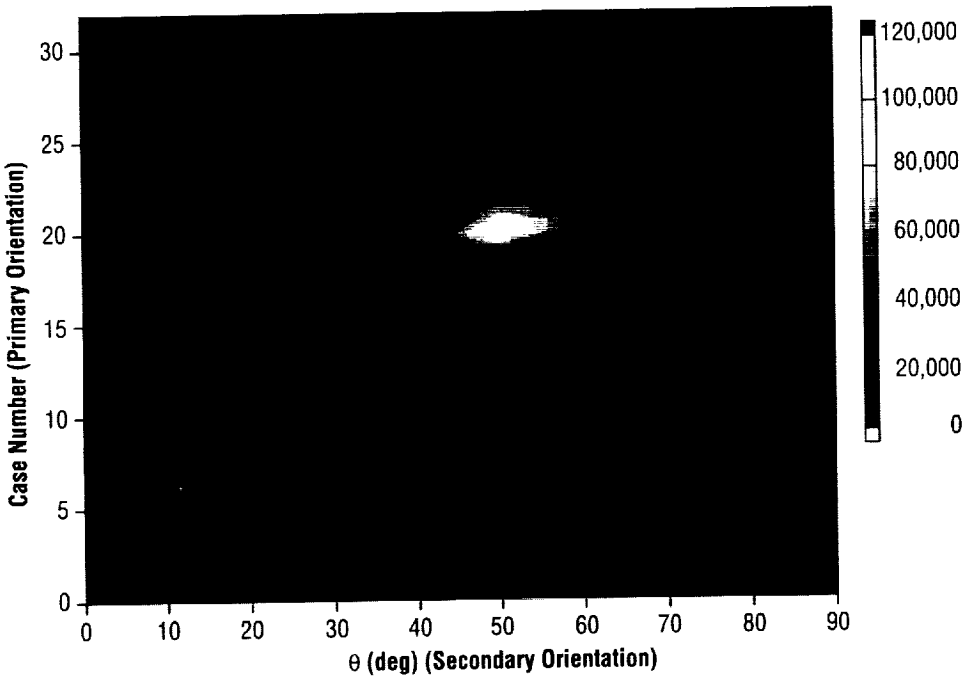

Figure 35. Dimensionless life contours at the blade dip critical point.

5.3.2 Stress Response in the Attachment Region (Frictionless Contact)

Blade attachment regions are prone to fretting fatigue crack initiation, as pointed out in section 3. Fretting occurs when assemblies of components such as blade and disk attachment surfaces are subjected to vibration, resulting in a contact damage process involving wear, corrosion, and fatigue phenomena driven by both the microslip at the contact surface and cyclic fretting contact stresses. The fretting contact surface is typically divided into a zone of microslip, where the surfaces experience relative motion on the order of 10–100 μm, and a region of no relative motion where the surfaces experience a condition of stick. The combined effects of corrosion, wear, and fatigue phenomena at the fretting contact facilitates the initiation and subsequent growth of cracks, ultimately leading to failure.

Contact surface stress for a critical point in the attachment region, shown in figure 31, is first examined with the assumption of zero friction. The critical point is located in the suction side upper contact region of the attachment, on the blade leading edge side (fig. 31). Effects of variation of primary and secondary orientation on stress response are studied for one FE nodal point (high stress critical contact point). Figure 36 shows a contour plot of $\Delta\tau_{max}$ as a function of primary and secondary orientation. The secondary orientation does not have any discernable effect at the contact point for this parameter. Figure 37 shows a contour plot of (τ_{max} $\Delta\varepsilon/2$) as a function of primary and secondary orientation. The secondary orientation does appear to have an optimum value of ≈55°. However, because of the complexity of state of stress in the contact region, failure parameters must be analyzed in greater detail. For both figures 37 and 38 the primary orientation, represented by case number, appears to be a strong factor in the calculated stress.

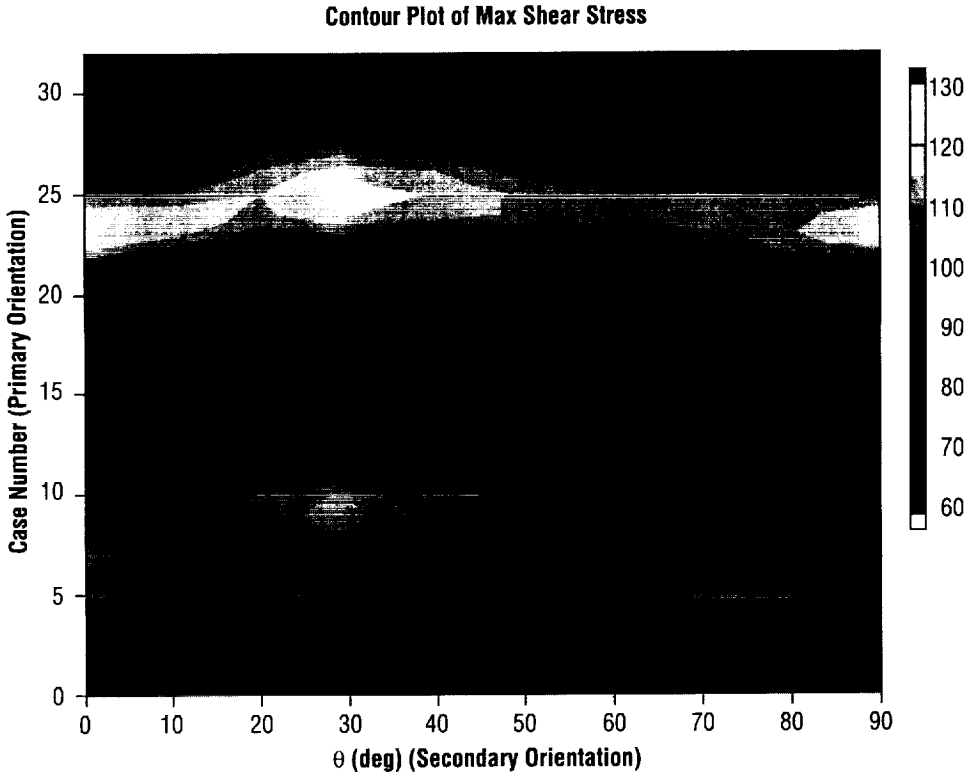

Figure 36. Maximum shear stress amplitude ($\Delta\tau_{max}$, ksi) contour at blade attachment point (frictionless contact).

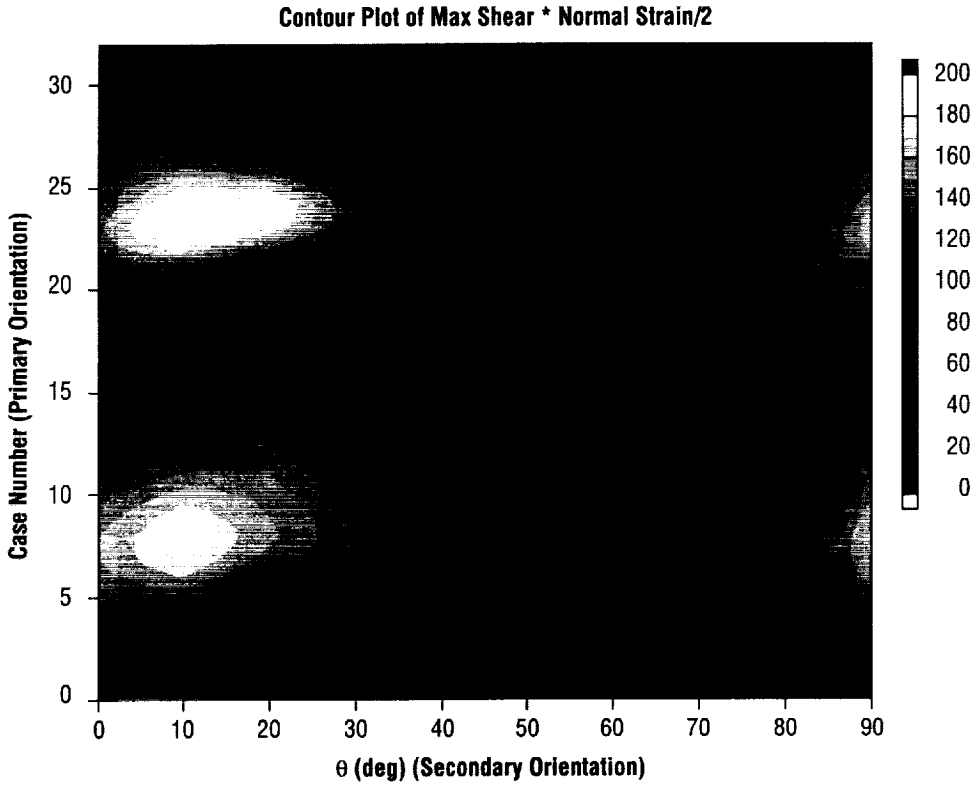

Figure 37. Contour of ($\tau_{max}\Delta\varepsilon/2$) contour at blade attachment critical point (frictionless contact).

5.3.3 Stress Response in the Attachment Region Including Contact Friction

The presence of friction results in the development of traction forces at the fretting contact. Evaluation of the contact forces and the resulting contact stresses at the interface requires careful analysis of the interaction between the contacting surfaces and applied loads. As explained earlier, the contacting nodes are modeled using CONTAC52 elements having 3 DOF at each node. This element allows development of tangential forces due to contact friction. The relative position and motion of the end nodes is used to define displacement and reaction force magnitude and direction.

To study the effect of variation of friction coefficient at the contact, and variation of primary and secondary crystal orientations, several three-dimensional FE model runs were completed. The case numbers shown in figure 30 and table 8 determine the primary orientation. The angle β determines the secondary orientation. Figure 38 and table 9 detail the results from 18 different three-dimensional FE model runs. The contact region shown in figure 38 is the same as that shown in figure 31. Table 9 shows the values used for primary orientation (cases 0, 5, and 30), secondary orientation (β=0 and 50°), and coefficient of friction (μ=0, 0.3, 0.7). Blade loading is kept constant for all 18 cases. Figure 38 shows a contour plot of tangential normal stress, σ_X, at the contact surface. The x coordinate is in the direction of slip, as shown in figure 31. The tangential normal stress is of practical interest because cracks are thought to initiate at locations where σ_X reaches a maximum tensile value. The maximum value of tangential normal stress, σ_X, reached in the contact zone is listed in table 9 for the 18 cases. It is seen that σ_X increases with μ. σ_X is also seen to vary considerably with variations in primary and secondary orientation. Since the component

stiffness varies with crystal orientation, the component stress distribution is also expected to vary under constant loads. Minimum values of σ_X are reached for case 30 and β=0 (84.3 ksi), indicating that key design parameters can be optimized for specific blade geometry and loading. Additional fretting damage parameters need to be examined for design optimization possibilities.

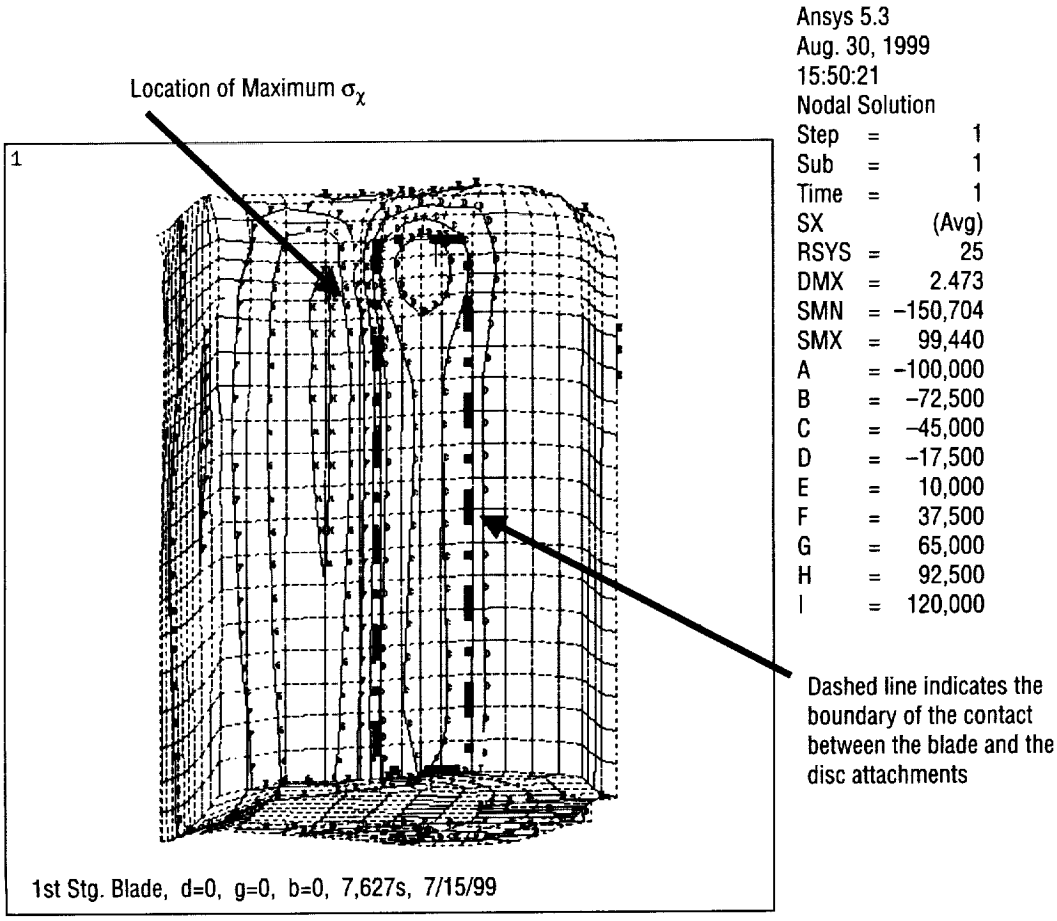

Figure 38. Case = 0, $\beta = 0$, $\mu = 0$, tangential surface stress in upper lobe, suction side, near leading edge.

Table 9. Values of crystal orientation, friction coefficient, and resulting stress.

Primary Orientation Case Number	Secondary Orientation β, deg	Friction Coefficient μ	Max σ_x (ksi)
0 (Δ=0, γ=0)	0	0.0	99.4
0	0	0.3	106.8
0	0	0.7	116.9
0	50	0.0	103.9
0	50	0.3	109.9
0	50	0.7	118.2
5 (Δ=0, γ=7.5)	0	0.0	105.7
5	0	0.3	113.1
5	0	0.7	123.3
5	50	0.0	108.6
5	50	0.3	114.4
5	50	0.7	122.6
30 (Δ=5.74, γ=–13.86)	0	0.0	84.3
30	0	0.3	89.9
30	0	0.7	97.7
30	50	0.0	94.1
30	50	0.3	98.8
30	50	0.7	105.2

Figures 39 and 40 show fretting/galling-induced cracks in the blade attachment region for HPFTP/AT first stage blades. The region shown in figure 39 is on the suction side, trailing edge of the blade. Several arrest marks are also visible. The blade crystal orientation is Δ=–6.7°, γ=11.3°, and β=4.2°. Figure 40 shows fretting/galling induced cracking showing multiple origins with stage II cracks. The crystal orientation for this blade is Δ=–2°, γ=3°, and β=7°. Many blades in different engine units exhibited similar blade attachment cracks. As pointed out earlier, the secondary orientation is not controlled, while the primary orientation is controlled to within 15°. A systematic investigation of severity of fretting/galling-induced attachment cracks, similar to the study shown in figure 33 for blade tip cracking, has to be done to discern relationships between fretting damage and crystal orientation. Figures 39 and 40 are included to illustrate representative fretting/galling damage in attachment regions. Tolerance in clearance between the blade and disk attachment surfaces also plays an important role in the contact stress distribution. The analysis results presented are for nominal clearances between mating parts.

A follow-up report will be published that deals with the variation of fretting stresses and strains (surface and subsurface) as a function of crystal orientation and coefficient of friction in greater detail.

Figure 39. Fretting/galling-induced crack in the contact region (suction side, trailing edge of blade). Several arrest marks are visible. Crystal orientation: $\Delta = -6.7°$, $\gamma = 11.3°$, $\beta = 4.2°$.

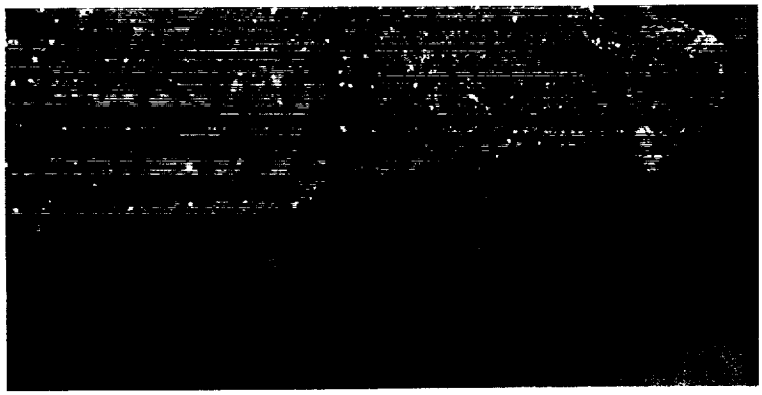

Figure 40. Fretting/galling-induced cracking showing multiple origins and stage II cracks (pressure side trailing edge location). Crystal orientation: $\Delta = -2°$, $\gamma = 3°$, $\beta = 7°$.

6. CONCLUSIONS

Fatigue failure in PWA 1480/1493, a single-crystal, Ni-based turbine blade superalloy, is investigated using a combination of experimental LCF fatigue data and three-dimensional FE modeling of HPFTP/AT SSME turbine blades. Several failure criteria, based on the normal and shear stresses and strains on the 24 octahedral and 6 cube slip systems for an FCC crystal, are evaluated for strain-controlled uniaxial LCF data (1,200 °F in air). The maximum shear stress amplitude [$\Delta\tau_{max}$] on the 30 slip systems was found to be an effective fatigue failure criterion, based on the curve fit between $\Delta\tau_{max}$ and cycles to failure. Since deformation mechanisms in single crystals are controlled by the propagation of dislocations driven by shear, $\Delta\tau_{max}$ might indeed be a good fatigue failure parameter to use. However, this parameter must be verified for a wider range of R-values and specimen orientations, and also at different temperatures and environmental conditions.

Investigation of leading edge tip cracks in operational SSME turbine blades had revealed that secondary crystal orientation appeared to influence whether a crack initiated and arrested or continued to grow until failure of the blade airfoil. The turbine blade was modeled using three-dimensional finite element analysis that is capable of accounting for material orthotrophy and variation in primary and secondary crystal orientation. Effects of variation in crystal orientation on blade stress response were studied based on 297 FE model runs. Fatigue life at the critical locations in blade was computed using FE stress results and failure criterion developed. Detailed analysis of the results revealed that secondary crystal orientation had a pronounced effect on fatigue life. The optimum value of secondary orientation β=50° computed corresponds very closely to the optimum value of β indicated in the failed population of blades. Control of secondary and primary crystallographic orientation has the potential to significantly increase a component's resistance to fatigue crack growth without adding additional weight or cost. Effect of crystal orientation and coefficient of friction on stress response in the blade attachment region is also investigated in view of its relevance to fretting/galling fatigue-induced failures.

REFERENCES

1. Cowles, B.A.: "High Cycle Fatigue Failure in Aircraft Gas Turbines: An Industry Perspective," *International Journal of Fracture*, Vol. 80, pp. 147–163, 1996.

2. Deluca, D.; and Annis, C.; "Fatigue in Single Crystal Nickel Superalloys," Office of Naval Research, Department of the Navy FR23800, August 1995.

3. Moroso, J.: "Effect of Secondary Crystal Orientation on Fatigue Crack Growth in Single Crystal Nickel Turbine Blade Superalloys," *M.S. Thesis*, Mechanical Engineering Department, University of Florida, Gainesville, FL, May 1999.

4. Stouffer, D.C.; and Dame, L.T.: *Inelastic Deformation of Metals*, John Wiley & Sons, 1996.

5. Milligan, W.W.; and Antolovich, S.D.: "Deformation Modeling and Constitutive Modeling for Anisotropic Superalloys," *NASA Contractor Report 4215*, February 1985.

6. Deluca, D.P.: Pratt & Whitney, Private Communication.

7. Deluca, D.P.; and Cowles, B.A.: "Fatigue and Fracture of Single Crystal Nickel in High Pressure Hydrogen," *Hydrogen Effects on Material Behavior*, N.R. Moody and A.W. Thomson (eds.), TMS, Warrendale, PA, 1989.

8. Telesman, J.; and Ghosn, L.: "The Unusual Near Threshold FCG Behavior of a Single Crystal Superalloy and the Resolved Shear Stress as the Crack Driving Force," *Engineering Fracture Mechanics*, Vol. 34, No. 5/6, pp. 1183–1196, 1989.

9. Telesman, J.; and Ghosn, L.: "Fatigue Crack Growth Behavior of Pwa 1484 Single Crystal Superalloy at Elevated Temperatures," International Gas Turbine and Aeroengine Congress and Exposition, June 1995.

10. John, R.; DeLuca, D.P.; Nicholas, T.; and Porter, J.: "Near-Threshold Crack Growth Behavior of a Single Crystal Ni-Base Superalloy Subjected to Mixed Mode Loading," *Mixed-Mode Crack Behavior*, ASTM STP 1359, K.J. Miller and D.L. McDowell (eds.), Paper ID: 5017, November 1998.

11. Findley, W.N.; Mather, P.N.; and Martin, D.E.: "Fatigue Failure Under Combinations of Stresses," Theoretical and Applied Mechanics Report No. 61, University of Illinois, 1954.

12. Kandil, F.A.; Brown, M.W.; and Miller, K.J.: *Biaxial Low Cycle Fatigue of 316 Stainless Steel at Elevated Temperatures*, Metals Soc., London, pp. 203–210, 1982.

13. Socie, D.F.; Kurath, P.; and Koch, J.: "A Multiaxial Fatigue Damage Parameter," presented at the Second International Symposium on Multiaxial Fatigue, Sheffield, U.K., 1985.

14. Fatemi, A.; and Socie, D.: "A Critical Plane Approach to Multiaxial Fatigue Damage Including Out-of-Phase Loading," *Fatigue Fracture in Engineering Materials*, Vol. 11, No. 3, pp. 149–165, 1988.

15. Smith, K.N.; Watson, P.; and Topper, T.M.: "A Stress-Strain Function for the Fatigue of Metals," *Journal of Materials*, Vol. 5, No. 4, pp. 767–778, 1970.

16. Banantine, J.A.; and Socie, D.F.: "Observations of Cracking Behavior in Tension and Torsion Low Cycle Fatigue," presented at ASTM Symposium on Low Cycle Fatigue—Directions for the Future, Philadelphia, 1985.

17. Lekhnitskii, S.G.: *Theory of Elasticity of an Anisotropic Elastic* Body, Holden-Day Inc., pp. 1–40, 1963.

18. Pratt and Whitney: "SSME Alternate Turbopump Development Program HPFTP Critical Design Review," PIW FR 24581–1, NASA Contract NAS8–36801, December 23, 1996.

19. Sayyah, T., "Alternate Turbopump Development Single Crystal Failure Criterion for High Pressure Fuel Turbopump First Stage Blades," Report No.: G21–025–99–001, NASA Contract NAS8–40836, May 27, 1999.

REPORT DOCUMENTATION PAGE

Form Approved
OMB No. 0704-0188

1. AGENCY USE ONLY *(Leave Blank)*	2. REPORT DATE	3. REPORT TYPE AND DATES COVERED
	February 2000	Technical Publication

4. TITLE AND SUBTITLE

Effect of Crystal Orientation on Analysis of Single-Crystal, Nickel-Based Turbine Blade Superalloys

5. FUNDING NUMBERS

6. AUTHORS

G.R. Swanson and N.K. Arakere*

7. PERFORMING ORGANIZATION NAMES(S) AND ADDRESS(ES)

George C. Marshall Space Flight Center
Marshall Space Flight Center, AL 35812

8. PERFORMING ORGANIZATION REPORT NUMBER

M–971

9. SPONSORING/MONITORING AGENCY NAMERS) AND ADDRESS(ES)

National Aeronautics and Space Administration
Washington, DC 20546–0001

10. SPONSORING/MONITORING AGENCY REPORT NUMBER

NASA/TP—2000–210074

11. SUPPLEMENTARY NOTES

Prepared by the Structures, Mechanics, and Thermal Department, Engineering Directorate
* University of Florida, Gainesville, Florida

12a. DISTRIBUTION/AVAILABILITY STATEMENT

Unclassified-Unlimited
Subject Category 39
Standard Distribution

12b. DISTRIBUTION CODE

13. ABSTRACT *(Maximum 200 words)*

High-cycle fatigue-induced failures in turbine and turbopump blades is a pervasive problem. Single-crystal nickel turbine blades are used because of their superior creep, stress rupture, melt resistance, and thermomechanical fatigue capabilities. Single-crystal materials have highly orthotropic properties making the position of the crystal lattice relative to the part geometry a significant and complicating factor. A fatigue failure criterion based on the maximum shear stress amplitude on the 24 octahedral and 6 cube slip systems is presented for single-crystal nickel superalloys (FCC crystal). This criterion greatly reduces the scatter in uniaxial fatigue data for PWA 1493 at 1,200 °F in air. Additionally, single-crystal turbine blades used in the Space Shuttle main engine high pressure fuel turbopump/alternate turbopump are modeled using a three-dimensional finite element (FE) model. This model accounts for material orthotrophy and crystal orientation. Fatigue life of the blade tip is computed using FE stress results and the failure criterion that was developed. Stress analysis results in the blade attachment region are also presented. Results demonstrate that control of crystallographic orientation has the potential to significantly increase a component's resistance to fatigue crack growth without adding additional weight or cost.

14. SUBJECT TERMS

single-crystal, nickel-based superalloy, high-cycle fatigue (HCF), PWA 1480, PWA 1484, PWA 1493, fatigue failure criteria

15. NUMBER OF PAGES

76

16. PRICE CODE

A05

17. SECURITY CLASSIFICATION OF REPORT	18. SECURITY CLASSIFICATION OF THIS PAGE	19. SECURITY CLASSIFICATION OF ABSTRACT	20. LIMITATION OF ABSTRACT
Unclassified	Unclassified	Unclassified	Unlimited

NSN 7540-01-280-5500

Standard Form 298 (Rev. 2-89)
Prescribed by ANSI Std. 239-18
298-102